FERMILAB-Pub-01/021-E

Production of π^0 and η mesons at large transverse momenta in pp and pBe interactions at 530 and 800 GeV/c

L. Apanasevich,[4] J. Bacigalupi,[1] W. Baker,[3] M. Begel,[9] S. Blusk,[8] C. Bromberg,[4] P. Chang,[5] B. Choudhary,[2] W. H. Chung,[8] L. de Barbaro,[9] W. DeSoi,[9] W. Długosz,[5] J. Dunlea,[9] E. Engels, Jr.,[8] G. Fanourakis,[9] T. Ferbel,[9] J. Ftacnik,[9] D. Garelick,[5] G. Ginther,[9] M. Glaubman,[5] P. Gutierrez,[6] K. Hartman,[7] J. Huston,[4] C. Johnstone,[3] V. Kapoor,[2] J. Kuehler,[6] C. Lirakis,[5] F. Lobkowicz,[9,‡] P. Lukens,[3] S. Mani,[1] J. Mansour,[9] A. Maul,[4] R. Miller,[4] B. Y. Oh,[7] G. Osborne,[9] D. Pellett,[1] E. Prebys,[9] R. Roser,[9] P. Shepard,[8] R. Shivpuri,[2] D. Skow,[3] P. Slattery,[9] L. Sorrell,[4] D. Striley,[5] W. Toothacker,[7,‡] N. Varelas,[9] D. Weerasundara,[8] J. J. Whitmore,[7] T. Yasuda,[5] C. Yosef,[4] M. Zieliński,[9] V. Zutshi[2]

(Fermilab E706 Collaboration)

[1] *University of California-Davis, Davis, California 95616*

[2] *University of Delhi, Delhi, India 110007*

[3] *Fermi National Accelerator Laboratory, Batavia, Illinois 60510*

[4] *Michigan State University, East Lansing, Michigan 48824*

[5] *Northeastern University, Boston, Massachusetts 02115*

[6] *University of Oklahoma, Norman, Oklahoma 73019*

[7] *Pennsylvania State University, University Park, Pennsylvania 16802*

[8] *University of Pittsburgh, Pittsburgh, Pennsylvania 15260*

[9] *University of Rochester, Rochester, New York 14627*

[‡] *Deceased*

(April 23, 2002)

Abstract

We present results on the production of high transverse momentum π^0 and η mesons in pp and pBe interactions at 530 and 800 GeV/c. The data span the kinematic ranges: $1 < p_T < 10\,\mathrm{GeV}/c$ in transverse momentum and 1.5 units in rapidity. The inclusive π^0 cross sections are compared with next-to-leading order QCD calculations and to expectations based on a phenomenological parton-k_T model.

PACS numbers: 12.38.Qk, 13.85.Ni

Typeset using REVTEX

I. INTRODUCTION

The study of inclusive single-hadron production at large transverse momentum (p_T) has been a useful probe in the development of perturbative quantum chromodynamics (PQCD) [1,2]. Early in the evolution of the parton model, a departure from an exponential dependence of particle production at lower p_T was interpreted in terms of the onset of interactions between pointlike constituents (partons) contained in hadrons. Large p_T is a regime where perturbative methods have been applied to QCD to provide quantitative comparisons with data. Such comparisons yield information on the validity of the PQCD description, and on parton distribution functions of hadrons and fragmentation functions of partons.

This paper reports high-precision measurements of the production of π^0 and η mesons with large p_T. The π^0 production cross sections are compared with next-to-leading order (NLO) PQCD calculations [3]. As illustrated in a previous publication [4], our data (for both inclusive π^0 and direct-photon production) are not described satisfactorily by the available NLO PQCD calculations, using standard choices of parameters. Similar discrepancies have been observed [5] between conventional PQCD calculations and other measurements of high-p_T π^0 and direct-photon cross sections (see also [6–8]). The origin of these discrepancies may be attributed to the effects of initial-state soft-gluon radiation. Such radiation generates transverse components of initial-state parton momenta, referred to below as k_T [9]. Evidence of significant k_T in various processes, and a phenomenological model for incorporating its effect on calculated high-p_T cross sections, have been extensively discussed in Refs. [4,5]; recent studies of the photoproduction of direct photons at HERA may provide additional insights [10–14]. The inadequacy of NLO PQCD in describing k_T-sensitive distributions has been discussed in Ref. [15]. In this paper, we follow the phenomenological prescription of Ref. [5] when comparing calculations with our π^0 data. We also present cross sections for η meson production at large-p_T. As might have been expected from earlier measurements (see, *e.g.*, [16]), η production, relative to π^0 production, shows little dependence on p_T or on

center of mass rapidity ($y_{\rm cm}$).

II. THE EXPERIMENTAL SETUP

The E706 experiment at Fermilab was designed to measure direct-photon production at high-p_T, and to investigate the structure of events containing direct photons. The data collection phase of the experiment spanned three fixed-target running periods, and included a relatively low statistics commissioning run in 1987-88 [16–19], and primary data runs in 1990 and 1991-92. The results presented here are from data recorded during the 1991-92 run. The E706 apparatus, operated in tandem with the E672 muon spectrometer, constituted the Meson West Spectrometer, displayed schematically in Fig. 1. The experiment used a right-handed Cartesian coordinate system, with the Z-axis pointed in the nominal beam direction, and the Y-axis pointed upward. The principal elements of the Meson West Spectrometer are discussed below. A more detailed description of the triggering methodology appears in Ref. [20].

A. Beamline and target

The Meson West beamline was capable of transporting either 800 GeV/c primary protons from the Fermilab Tevatron or secondary beams of either polarity. We report here on results from studies using 800 GeV/c primary protons and a 530 GeV/c positive secondary beam. The beamline was instrumented with a differential Čerenkov counter [21,22] to identify incident pions, kaons, and protons in secondary beams. This helium-filled counter was 43.4 m long and was located ≈100 m upstream of the experiment's target. Using the Čerenkov counter, the proton fraction at 530 GeV/c was determined to be 97% [21].

A 4.7 m long stack of steel surrounding the beam pipe was placed between the last beamline magnet and the target box (see Fig. 1) to absorb hadrons. A water tank was placed at the downstream end of this hadron shield to absorb low-energy neutrons. During the 1991-92 run, two walls of scintillation counters were located both upstream and downstream of

the hadron shield to identify penetrating muons.

The target region during the 1991-92 run consisted of two 0.8 mm thick copper disks of 2.5 cm diameter, located immediately upstream of a liquid hydrogen target, followed by a 2.54 cm long beryllium cylinder of diameter 2.54 cm. The hydrogen target consisted of a 15 cm long mylar flask, supported in an evacuated volume, with beryllium windows at each end (2.5 mm thickness upstream and 2.8 mm thickness downstream) [23].

B. Charged particle tracking

The spectrometer employed a charged particle tracking system consisting of silicon strip detectors (SSDs) [24], a dipole analysis magnet, proportional wire chambers (PWCs), and straw tube drift chambers (STDCs) [25]. The SSD system consisted of sixteen planes of silicon wafers, arranged in eight modules. Each module contained two SSD planes, one providing X-view information and the other instrumenting the Y-view. Six 3×3 cm^2 SSD planes were located upstream of the target and used to reconstruct beam tracks. Two hybrid 5×5 cm^2 SSD planes (25 μm pitch strips in the central 1 cm, 50 μm beyond) were located $\approx$2 cm downstream of the Be target [26]. These were followed by eight 5×5 cm^2 SSD planes of 50 μm pitch. The SSDs were instrumented to cover a solid angle of ±125 mr. Figure 2 displays the distribution of reconstructed vertices from a representative sample of 1991-92 data, showing clear separation of the different target elements.

The analysis dipole magnet imparted a transverse momentum impulse of $\approx$450 MeV/c (in the horizontal plane) to singly-charged particles. Downstream track segments were measured by means of four stations of four views ($XYUV$) of 2.54 mm pitch PWCs and two stations of eight ($4X4Y$) layers of STDCs with tube diameters 1.03 cm (upstream station) and 1.59 cm (downstream station). The STDC stations were installed prior to the 1990 fixed-target run, and improved the angular resolution of the downstream tracking system (to $\approx$0.06 mrad) to make it comparable to that of the upstream system.

C. Calorimetry

The central element of the E706 apparatus was the finely-segmented liquid argon electromagnetic calorimeter (EMLAC) used to detect and measure electromagnetic showers [27,28]. The EMLAC had a cylindrical geometry with an inner radius of 20 cm and an outer radius of 160 cm. It was divided into four mechanically independent quadrants, which were further subdivided electronically to create octants. The calorimeter had 33 longitudinal cells read out in two sections: an 11 cell front section ($\approx$8.5 radiation lengths) and a 22 cell back section ($\approx$18 radiation lengths). This front/back split was used for measuring the direction of incidence of showering particles, for discriminating between electromagnetic and hadronic showers and for resolving closely separated electromagnetic showers. The longitudinal cells consisted of 2 mm thick lead cathodes (the first cathode was constructed of aluminum), double-sided copper-clad G-10 radial (R) anode boards, followed by 2 mm thick lead cathodes and double-sided copper-clad G-10 azimuthal (Φ) anode boards. There were 2.5 mm argon gaps between each of these layers in a cell. The physical layout is illustrated in Fig. 3.

The copper-cladding on the anode boards was cut to form strips. Signals from corresponding strips from all R (or Φ) anode boards in the front (or back) section were jumpered together. The copper-cladding on the radial anode boards was cut into concentric strips centered on the nominal beam axis. The width of the strips on the first R board was 5.5 mm. The width of the R strips on the following R boards increased slightly so that the radial geometry was projective relative to the target, which was located 9 m upstream of the EMLAC. The azimuthal readout was subdivided at a radius of 40 cm into inner and outer segments, with each inner Φ strip subtending an azimuthal angle of $\pi/192$ radians, and outer Φ strips covering $\pi/384$ radians. Subdivision of the azimuthal strips in the outer portion of the detector improved both the position and energy resolution for showers reconstructed in this region. It also reduced R–Φ correlation ambiguities from multiple showers in the same octant of the calorimeter.

Data acquisition and trigger-signal processing for the EMLAC was based upon the FNAL

RABBIT system [29]. To achieve tolerable deadtimes, the zero suppression features of this system were used extensively during the experiment's 1987-88 commissioning run. However, zero suppression limited our ability to understand the effects of out-of-time photon-induced showers and the tails of hadron-induced showers, thereby compromising efforts to understand the detailed response of the detector. Consequently, FASTBUS modules (the ICBM—Intelligent Control and Buffering Module—and the Wolf interface [30,31]) were developed by E706 to replace the original, CDF-designed, MX readout controllers. These FASTBUS modules enabled us to eliminate zero suppression during the experiment's two primary data runs.

The apparatus also included two other calorimeters: a hadronic calorimeter (HALAC) located downstream of the EMLAC in the same cryostat, and a steel and scintillator calorimeter (FCAL), positioned further downstream, to increase coverage in the very forward region. The HALAC had 53 longitudinal cells read out in 2 sections: a 14 cell front section ($\approx$2 interaction lengths), and a 39 cell back section ($\approx$6 interaction lengths). Each cell consisted of read-out planes separated by 3 mm argon gaps and a 2.5 cm thick steel plate.

The FCAL acceptance covered the beam hole region of the EMLAC. It was split into three longitudinally similar sections. Each section was composed of alternating layers of 1.9 cm thick steel absorber plates and 4.8 mm thick acrylic scintillator sheets. The distance between steel plates was 6.9 mm. The downstream module contained 32 steel absorber plates and 33 scintillator sheets; the other two modules were comprised of 28 steel absorber plates and 29 scintillator sheets. Together, the three modules constituted $\approx$10.5 interaction lengths of material.

D. Muon identification

The E672 muon spectrometer, consisting of a toroidal magnet, shielding, scintillators, and proportional wire chambers, was deployed immediately downstream of the FCAL. The combined Meson West Spectrometer was triggered on high-mass muon pairs in order to

investigate the hadroproduction of J/ψ, $\psi(2s)$, χ_c, and B mesons [32–35]. E706 and E672 collected data simultaneously and shared trigger logic, the data acquisition system, and event reconstruction programs. Data collected with the dimuon trigger were also used for several technical studies—for example, the $J/\psi \longrightarrow \mu^+\mu^-$ signal was used to calibrate the momentum scale of the tracking system.

E. Triggering

The E706 trigger selected events yielding high transverse momentum showers in the EMLAC. The selection process involved four stages: beam and interaction definitions, pretrigger requirements, and the final trigger requirements. Beam particles were detected using a hodoscope consisting of three planes (arranged in X, Y and U views) of scintillator, located $\approx$2 m upstream of the target region. Each plane contained 12 scintillator strips. The widths of the strips varied from 1 mm in the central region, to 5 mm along the edges. The edges of individual strips in each plane were overlapped to avoid gaps in acceptance. A BEAM signal was generated by a coincidence of signals from counters in at least two of the three hodoscope planes. A BEAM1 signal required that less than two hodoscope planes detected two or more isolated clusters of hits in coincidence with BEAM. This BEAM1 requirement rejected events with multiple beam particles incident upon the target. A plane of four scintillation counters (referred to as beam hole counters) arranged to produce a 0.95 cm diameter central hole was located downstream of the beam hodoscope and used to reject interactions initiated by particles in the beam halo.

Two pairs of scintillation counters were mounted on the dipole analysis magnet, one pair upstream and the other downstream of the magnet. Each pair had a central hole that allowed non-interacting beam particles to pass through undetected. An INTERACTION was defined as a coincidence between signals from at least two of these four interaction counters. To minimize potential confusion in the EMLAC due to out-of-time interactions, a filter was used to reject interactions that occurred within 60 ns of one other.

For those interactions that satisfied both the BEAM1 and INTERACTION definitions, the p_T deposited in various regions of the EMLAC was evaluated by weighting the energy signals from the fast outputs of the EMLAC R channel amplifiers by $\approx\sin\theta_i$, where θ_i is the polar angle that the ith strip subtends with respect to the nominal beam axis. The PRETRIGGER HI requirement was satisfied when the p_T detected either in the inner 128 R channels or the outer R channels of any octant was greater than the threshold value of $\approx$2 GeV/c. A pretrigger signal was issued only if the signals from a given octant satisfied the pretrigger requirement, there was no evidence in that octant of substantial noise or significant p_T attributable to an earlier interaction, and there was no incident beam halo muon detected by the walls of scintillation counters surrounding the hadron shield upstream of the spectrometer. The pretrigger signal latched data from the various subsystems until a final trigger decision was made.

Localized trigger groups were formed for each octant by clustering the R channels into 32 groups of 8 channels. Each of the adjacent pairs of 8 channel groups (groups 1 and 2, 2 and 3, ... , 31 and 32) formed a LOCAL group of 16 strips. If the p_T detected in any of these groups of 16 was above a specified high (or low) threshold, then a LOCAL HI (or LOCAL LO) signal was generated for that octant. The SINGLE LOCAL HI (SINGLE LOCAL LO) trigger required a LOCAL HI (LOCAL LO) signal from an octant that also satisfied the PRETRIGGER HI. The LOCAL HI (LOCAL LO) threshold was $\approx$3.5 GeV/c ($\approx$2 GeV/c). The SINGLE LOCAL LO trigger was prescaled by a factor of $\approx$200.

In addition to these high-p_T triggers, prescaled samples of low-bias BEAM, INTERACTION, and pretrigger events were also recorded. The prescale factors for these triggers were typically set at 15^6, 15^5, and 15^3, respectively. These low-bias triggers constituted $\approx$10% of the events recorded.

III. π^0 AND η ANALYSIS

The data sample used in this analysis corresponds to an integrated luminosity of 6.8 (1.2) events/pb for 530 GeV/c pBe (pp) interactions, and 6.5 (1.2) events/pb at 800 GeV/c. The following subsections describe the analysis procedures and methods used to correct the data for losses resulting from inefficiencies and selection biases.

A. Event reconstruction

The charged-track reconstruction algorithm produced track segments upstream of the dipole magnet using information from the SSDs, and downstream of the magnet using information from the PWCs and STDCs. These track segments were projected to the center of the magnet, and linked to form the final tracks, and the interaction vertex. The charged-track reconstruction and vertex-finding methodology are described in Ref. [20].

The readout in each EMLAC quadrant consisted of four regions: left R and right R (radial strips of each octant in that quadrant), and inner Φ and outer Φ regions (azimuthal strips divided at $R = 40$ cm). Strip energies from clusters in each region were fitted to the shape of electromagnetic showers, as determined from Monte Carlo simulations and isolated-shower data. These fits were used to evaluate the positions and energies (E_R and E_Φ) of the peaks in each region. Shower positions and energies were obtained by correlating peaks of approximately the same energy in the R and Φ regions within the same half octant (more complex algorithms were used to handle configurations with overlapping showers in either the R or Φ regions). Any differences in photon energy as measured in the R and Φ views reflect the intrinsic resolution properties of the calorimeter, and provide a test of the quality of the Monte Carlo simulations. The EMLAC's longitudinal segmentation provided discrimination between showers generated by electromagnetically or hadronically interacting particles. For individual showers, the ratio of energy reconstructed in the front section to the sum of energy in the front and back section of the EMLAC (referred to as $E_{\rm FRONT}/E_{\rm TOTAL}$)

also tested the Monte Carlo simulation of longitudinal shower development (see the detector simulation section below). An expanded discussion of the EMLAC reconstruction procedures and performance can be found in Ref. [28].

B. Data sample selection and corrections

The events contributing to the cross section measurements were required to have a reconstructed vertex within the fiducial volume of the Be or H_2 targets [36]. Vertex reconstruction efficiencies were evaluated for each target using a detailed Monte Carlo simulation of the spectrometer (described below). These efficiencies were used to correct for reconstruction losses and for resolution smearing across target fiducial boundaries. The vertex reconstruction efficiency was ≈ 1 for the H_2 and downstream Be targets and 0.97 for the upstream Be target.

Both π^0 and η mesons were reconstructed via their $\gamma\gamma$ decay modes. The photons were required to be within the fiducial region of the EMLAC, which excluded areas with reduced sensitivity. In particular, photons incident upon regions of the detector near quadrant boundaries (which abutted steel support plates), the central beam hole, the outer radius of the EMLAC, and octant boundaries were excluded from consideration. A simple ray-tracing Monte Carlo program was employed to determine the correction for the effect of the azimuthal fiducial boundaries [37].

To reduce backgrounds from hadronic showers, only showers with at least 20% of their shower energy deposited in the front part of EMLAC ($E_{\rm FRONT}/E_{\rm TOTAL} > 0.2$) were accepted as photon candidates. To correct the cross sections for this requirement, as well as for other larger effects including resolution-smearing and reconstruction losses, a full simulation of the showers in the calorimeter (described below) was employed. In addition, $\gamma\gamma$ combinations were considered as π^0 or η candidates only when the two photons were detected in the same octant (to simplify subsequent analysis of the trigger response), and only those combinations with energy asymmetry $[A_{\gamma\gamma} \equiv |E_{\gamma_1} - E_{\gamma_2}|/(E_{\gamma_1} + E_{\gamma_2})]$ less than 0.75 were considered (to

reduce uncertainties due to low energy photons).

The $\gamma\gamma$ invariant mass distribution in the π^0 and η regions for photon pairs that satisfied the above requirements is shown in Fig. 4 for representative low p_T intervals. A π^0 candidate was defined as a combination of two photons with invariant mass, $M_{\gamma\gamma}$ [38], in the range $100\ \mathrm{MeV}/c^2 < M_{\gamma\gamma} < 180\ \mathrm{MeV}/c^2$. An η candidate was defined as a two-photon combination in the range $450\ \mathrm{MeV}/c^2 < M_{\gamma\gamma} < 650\ \mathrm{MeV}/c^2$. To evaluate production cross sections, combinatorial background in the π^0 and η regions was evaluated as follows. Sideband regions were defined to cover an equivalent mass range of the π^0 and η peak regions (using the same acceptance criteria as for the peak regions). The p_T and rapidity distributions from these side bands were then subtracted from the corresponding distributions within the π^0 and η mass ranges to obtain the respective signals. This technique is appropriate as long as the combinatorial background depends approximately linearly dependence on $M_{\gamma\gamma}$. At low p_T (below ≈ 2 GeV/c), the shape of the combinatorial background in the signal regions is not linear, and a more sophisticated fitting procedure was used to evaluate the background. The $\gamma\gamma$ mass distributions were fitted to Gaussians for signal plus second-order polynomials in $M_{\gamma\gamma}$ to represent the background. The combinatorial background in the peak regions was then defined using the resultant parameters of the fit, and the signals defined as the differences between the totals and the fitted backgrounds.

For the cross section measurements, the signals have been corrected for losses due to the energy asymmetry cut and the branching fractions [39] for the $\gamma\gamma$ decay modes. The correction for losses due to the conversion of one or both of the photons into e^+e^- pairs was evaluated by projecting each reconstructed photon from the event vertex to the reconstructed position in the EMLAC. The number of radiation lengths of material traversed along the photon path was calculated on the basis of a detailed description of the detector. The photon conversion probability was then evaluated and used to account for losses from conversion.

C. Trigger response

As mentioned previously, the SINGLE LOCAL HI and SINGLE LOCAL LO trigger decisions were based upon depositions of p_T in the EMLAC within groups of 16 contiguous radial strips. For each π^0 or η candidate, a probability to satisfy the trigger was defined, based upon energy deposition in the entire octant, as $P = 1 - \prod(1 - p_i)$, where p_i is the efficiency of the ith trigger group in the octant containing the candidate [40]. The inverse of this probability was applied as a trigger weight to each meson candidate. To avoid excessively large trigger weights, meson candidates with trigger probabilities of < 0.1 were excluded from further consideration. The correction for losses from this requirement was determined from Monte Carlo, and absorbed into the reconstruction efficiency.

The efficiency of the PRETRIGGER HI was determined in a manner similar to that used for the local triggers [40]. Additional details on the trigger can be found in Refs. [20,41,42].

The cross sections presented in this paper reflect composite measurements, utilizing a combination of results from the INTERACTION, PRETRIGGER HI, SINGLE LOCAL LO, and SINGLE LOCAL HI triggers. The p_T spectra (corrected for only prescale factors) from a representative sample of these triggers are shown in Fig. 5. The transition points chosen between the high and low threshold triggers were determined by comparing the fully corrected results from each trigger, and were different for π^0 and η mesons and also depended on rapidity.

D. Rejection of beam halo muons

Spurious triggers were produced by muons in the beam halo that radiated energy in the electromagnetic calorimeter in random coincidence with an interaction in the target. Particularly in the outer regions of the EMLAC, this energy was recorded as a high-p_T deposition that satisfied the LOCAL trigger requirements. This occurred much more frequently in data from the 530 GeV/c secondary beam than for the primary 800 GeV/c beam, due to the absence of an upstream interaction target in the latter case. To reduce this background,

the pretrigger logic relied on signals from the veto walls of scintillator counters to reject events associated with such muons in the beam halo. In the off-line analysis, we employed expanded requirements on the latched veto-wall signals, the direction of reconstructed showers [28], the shower shape (halo muon-induced showers have a different shape than photon or electron-induced showers), and the total p_T (balance) in the event. For the latter, we calculated the net p_T of the photons and charged particles which, based upon their initial trajectories, would intercept the EMLAC in the transverse plane within the 120° sector opposite the meson candidate. In interactions which generate a high-p_T meson, the ratio of this "away-side" p_T (P_T^{away}) to that of the meson p_T should be near unity. However, for events triggered by showers from beam halo muons, P_T^{away}/p_T should be near zero, since the interaction in random coincidence with the beam halo muon is typically a soft (low p_T) interaction. Candidates with $P_T^{away}/p_T < 0.3$ were considered likely to be due to beam halo muons and were rejected.

To illustrate the effect of the above off-line requirements, the $\gamma\gamma$ invariant mass distribution, both before and after application of the rejection criteria, is shown in Fig. 6 for the 530 and 800 GeV/c data, for $p_T > 7.0$ GeV/c. The large muon-induced background at low $\gamma\gamma$ mass values in the 530 GeV/c data is due to the occasional transverse splitting of the muon-induced showers into two closely-separated photon candidates. This happens because the reconstruction software assumes that the showers originate from the target-region rather than from the beam halo. The 800 GeV/c data have very few muon-induced triggers, and is consequently not affected very strongly by these rejection criteria.

The impact of these rejection criteria on the physics signal was checked using more restrictive selection criteria to define a pure sample of $\gamma\gamma$ pairs. The fraction of signal lost by the application of each of the muon-rejection requirements determined a correction to the cross section. The product of the correction factors for muon rejection corresponds to an increase of ≈8% in the cross secton at $p_T = 4$ GeV/c, and ≈10% at $p_T = 7$ GeV/c, for the 530 GeV/c beam data. (The corrections were smaller for the 800 GeV/c data because of cleaner beam conditions.)

E. Detector simulation

The Meson West spectrometer was modeled using a detailed GEANT [43] simulation. Because the full simulation of electromagnetic showers requires extensive computing time, we developed a hybrid approach using GEANT-tracking through the magnetic spectrometer and in the initial stages of the shower development in the calorimeter. We used the standard GEANT algorithms for tracking particles with energies above 10 MeV, below which we relied on an empirical parameterization for the deposition of energy in the EMLAC [44]. This cutoff was selected to be at the point at which bremsstrahlung still dominates the energy loss in lead, and led to significant improvement in processing speed. In doing this, we took advantage of the steady advances in computational power of the FNAL UNIX farms [45] to reach the desired level of statistical accuracy.

As inputs to the GEANT simulation, we employed single particle distributions, reconstructed data events, and two physics event generators: HERWIG [46] and PYTHIA [47]. For the analyses described herein, we chose HERWIG as the principal Monte Carlo event generator based on a better match of particle multiplicities between data and Monte Carlo using the default parameters. Over 5.5 million HERWIG events were passed through the GEANT simulation. We weighted the HERWIG π^0 and η spectra (in p_T and rapidity) to match our measured results, so that the corrections obtained from the Monte Carlo were based on the data distributions rather than on the behavior of the physics generator.

The calibration of the energy response of the EMLAC was based on the reconstructed masses of π^0 mesons in the $\gamma\gamma$ decay mode [28]. The steeply falling p_T spectrum for π^0 production, combined with the calorimeter's resolution, produced a small offset ($\approx$1%) in the mean reconstructed photon energies. Using the same calibration procedure in the simulated EMLAC as in the detector, we corrected this offset and minimized any potential biases in the calibration. We also employed the GEANT Monte Carlo simulation to evaluate the mean correction (as a function of photon energy) for energy deposited in the material upstream of the EMLAC. The impact of detector resolution on the energy scale and on the π^0 and η

production spectra was incorporated in the overall reconstruction efficiency corrections.

To ensure that the Monte Carlo simulation reproduced the data, a special preprocessor was used to convert GEANT information into signals and strip energies as measured in the various detectors, and to simulate hardware effects, such as channel noise and gain variations. The generated Monte Carlo events were then processed through the same reconstruction software used for the analysis of data, and thereby provided measures of the inefficiencies and biases of the reconstruction algorithms.

Comparisons between results from the Monte Carlo simulation and the data for the distributions in $E_R - E_\Phi$ and in the fraction of energy deposited in the front section of the EMLAC, $E_{\rm FRONT}/E_{\rm TOTAL}$, are presented in Figs. 7 and 8. The Monte Carlo results are in satisfactory agreement with the data, indicating that the simulation properly treats shower development in the EMLAC. Figures 9 and 10 show the $\gamma\gamma$ mass spectra in the π^0 and η mass regions for two minimum-p_T requirements, and compare these spectra to the Monte Carlo simulation. In addition to giving further evidence that the Monte Carlo provides a good simulation of the resolution of the EMLAC, the agreement in the levels of the combinatorial background indicates that the Monte Carlo also provides reasonable simulation of the underlying event structure. Figure 11 shows a comparison between the Monte Carlo and the data for the sideband-subtracted π^0 energy asymmetry distribution, and the agreement indicates that the Monte Carlo simulation describes accurately the losses of low-energy photons.

Reconstruction inefficiencies for π^0 and η mesons (which satisfied the $A_{\gamma\gamma}$, energy asymmetry, requirement) were relatively small over most of the kinematic range. Figure 12 shows the probability for a π^0 to pass the selection requirements imposed on the Monte Carlo events at 530 GeV/c, as a function of p_T, for different rapidity intervals. This probability includes losses due to the reconstruction algorithm, the $E_{\rm FRONT}/E_{\rm TOTAL}$ requirement, and the 10% minimum trigger probability requirement. The inefficiency at forward rapidities and high-p_T is attributable to the increased difficulty in separating two photons from π^0 decays (coalescence) in this kinematic region.

F. Normalization

Electronic scalers that counted signals from the beam hodoscope, interaction counters, and beam hole counters were used to determine the number of beam particles incident on the target. Other scalers logged the state of the trigger and of components of the data acquisition system. Information from these scalers was used to determine the number of beam particles that traversed the spectrometer when it was ready to record data. This number was corrected for multiple occupancy in the beam hodoscope (beyond that excluded via the BEAM1 requirement, and for absorption of beam in the target material.

The normalization of the low p_T π^0 cross section was independently verified using events from the prescaled BEAM and INTERACTION trigger samples. In these samples, the absolute normalization can be obtained just by counting events. For these low p_T events, the normalization as determined via the scalers and via event counting techniques agree to better than 3%.

Based upon the good agreement between results from these independent normalization methods, combined with the stability of the cross section results from various sections of the run, an evaluation of the internal consistency of the scalers, and a detailed analysis of the design, implementation and performance of the trigger, the net systematic uncertainty in the overall normalization is $\approx$8%.

G. Secondary Beam Contamination

The 530 GeV/c secondary beam cross section measurements were corrected for the small admixture of pions and kaons present in the beam, estimated as 2.75% π^+ and 0.5% K^+, respectively [21]. Although the percentage contamination is small, it's effect at high p_T is enhanced by the presence of two, rather than three, valence quarks in incident mesons. The effect of π^+ contamination was estimated using our high statistics study of π^0 and η meson production by 515 GeV/c π^- beam [4,48]. This is justified because: neutral meson

production by π^+ and π^- beams is expected to be similar, based on isospin arguments and earlier measurements [49]; the π^+ component of the nominally 530 GeV/c positive secondary beam had a mean momentum of 515 GeV/c; and the ratio of the measured high p_T π^0 cross section from the Čerenkov-tagged π^+ component of the positive secondary beam to the corresponding cross section from the 515 GeV/c π^- beam was consistent with unity [21].

The effect of K^+ contamination was assumed to be half that of the same amount of π^+ contamination, consistent with earlier, lower energy measurements [50] and with our own, more statistically limited, data [21]. After correcting for beam contamination, the 530 GeV/c cross sections were reduced by $\approx 2\%$ at low p_T and by $\approx 10\%$ at high p_T.

H. Summary of systematic uncertainties

The principal contributions to the systematic uncertainty arose from the following sources: calibration of photon energy response (5–9%), π^0 and η reconstruction efficiency and detector-resolution unsmearing (5%), the overall normalization (8%), and, for the 530 GeV/c secondary beam, the beam contamination (0–7%). A more complete list of systematic uncertainties is presented in Table I. Some of these uncertainties (*e.g.* normalization) are strongly correlated between bins. The systematic uncertainties, combined in quadrature, are quoted with cross sections in the appropriate tables. Combining all systematic uncertainties yields a net uncertainty that varies from 11% (13%) at low p_T for π^0 (η) mesons to 15% at high-p_T.

The secondary proton beam was determined to have a mean momentum of 530 ± 2 GeV/c with an estimated halfwidth of ≈ 30 GeV/c. This momentum spread introduces a small uncertainty ($\approx 5\%$) in comparisons of theory with data. (For the 800 GeV primary beam, the momentum bite and the corresponding uncertainty are negligible.)

IV. INCLUSIVE CROSS SECTIONS

A. π^0 production

The inclusive π^0 cross sections per nucleon versus p_T are shown in Figs. 13 and 14 for 530 and 800 GeV/c proton beams, respectively, incident upon beryllium and liquid hydrogen targets. Because of the steeply falling spectra, the data are plotted at abscissa values that correspond to the average values of the cross section in each p_T bin (assuming local exponential p_T dependence) [51]. These cross sections are also tabulated in Tables II and III. The corresponding cross section measurements, as functions of p_T and $y_{\rm cm}$ are reported in Tables IV through VII.

NLO PQCD calculations [3] are compared to the data in Figs. 15 through 23. In Fig. 15, NLO PQCD results using CTEQ4M parton distribution functions [52] and BKK fragmentation functions [53] are compared to the measured inclusive π^0 cross sections for pBe and pp interactions at 800 GeV/c. The PQCD calculations for the Be target have been adjusted to account for nuclear effects by the factor $A^{\alpha-1}$, where A is the atomic number and α = 1.12 (1.08) for 530 (800) GeV/c incident protons. Theoretical results are presented for three values of the factorization scale: $\mu = p_T/2$, p_T, and $2p_T$. (In these comparisons, the renormalization and fragmentation scales have been set to the value of the factorization scale.) In addition to a large dependence on the choice of scale, the expectations for these choices of μ lie significantly below the data, at both 530 and 800 GeV/c.

In Fig. 16, NLO calculations using BKK and KKP [54] fragmentation functions, and $\mu = p_T/2$, are compared to the π^0 cross sections for 530 GeV/c pBe and pp interactions. The calculations exhibit considerable dependence on the choice of fragmentation function, but both choices predict yields that are significantly lower than the data.

These discrepancies have been interpreted [4–6] as arising from additional soft-gluon emission in the initial state that is not included in the NLO calculation, and which results in sizeable parton k_T before the hard collision (for a different perspective, see the discus-

sion in Ref. [8]). Soft-gluon (or k_T) effects are expected in all hard-scattering processes, such as the inclusive production of jets, high-p_T mesons, and direct photons [55–58]. The Collins-Soper-Sterman resummation formalism [59] provides a rigorous basis for understanding these radiation effects, and there have been several recent efforts to derive resummation descriptions for the inclusive direct-photon [60–63] and dijet cross sections [64–66]. The calculation of Ref. [60] for inclusive direct-photon production, which includes the effects of soft-gluon resummation near the kinematic threshold limit ($x_T = 2p_T/\sqrt{s} \longrightarrow 1$), has a far smaller sensitivity to scale, compared to NLO calculations, and provides cross sections close to those of NLO calculations with a scale of $\mu = p_T/2$. Also, for our energies, the calculation of Ref. [67] using k_T-resummation, and of Ref. [63], which treats simultaneously threshold and recoil effects in direct-photon production, yield a substantially larger cross section than the NLO result. However, no such calculations are available for inclusive meson production. In their absence, we use a PQCD-based model that incorporates transverse kinematics of initial-state partons to study the principal consequences of additional k_T for high-p_T production processes.

Because the unmodified PQCD cross sections fall rapidly with increasing p_T, the net effect of the "k_T smearing" is to increase the expected yield at higher p_T's. An exact treatment of the modified parton kinematics has been implemented in a Monte Carlo calculation of the leading-order (LO) cross sections for high-p_T particle production [68], with the k_T distribution for each of the incoming partons represented by a Gaussian with one adjustable parameter ($\langle k_T \rangle$). Unfortunately, no such program is available for NLO calculations, and so we approximate the effect of k_T smearing by multiplying the NLO cross sections by the corresponding LO k_T-enhancement factors. Admittedly, this procedure involves a risk of double-counting since some of the k_T-enhancement may already be contained in the NLO calculation. However, we expect such double-counting effects to be small.

The $\langle k_T \rangle$ values used in the calculation of the LO k_T-enhancement factors are similar to those employed in comparisons of kinematic distributions in data involving production of high-mass $\gamma\gamma$, $\gamma\pi^0$, and $\pi^0\pi^0$ systems with calculations relying on the same LO program

(see Refs. [4,5] for further details). For these comparisons, we used the LO versions of the CTEQ4 distribution and (where appropriate) BKK fragmentation functions, and an average transverse momentum of 0.6 GeV/c for the π^0 mesons relative to the fragmenting parton direction (varying this parameter in the range 0.3 to 0.7 GeV/c does not affect our conclusions) [69,70].

Comparisons of the k_T-enhanced calculations with data at 530 GeV/c are displayed in Fig. 17, indicating reasonable agreement for the $\langle k_T \rangle$ values chosen. Similar conclusions can be drawn from comparisons between calculations and data at 800 GeV/c, as illustrated in Fig. 18. It is interesting to compare the fractional differences between data and the k_T-enhanced NLO calculations using BKK and KKP fragmentation functions on a linear scale. Such comparisons are shown in Fig. 19 for pBe interactions at 530 and 800 GeV/c. The k_T-enhanced calculations using the KKP fragmentation functions are seen to reproduce the shape of the π^0 cross section better than calculations using the earlier BKK fragmentation functions, but small discrepancies are still present. Similar conclusions can be drawn from comparisons of NLO QCD with our data on pp collisions (Fig. 20), although in this case the fractional differences using the KKP fragmentation functions are systematically greater than zero when we employ the same $\langle k_T \rangle$ values used in Fig. 19. It is, however, worth noting that the hydrogen nucleus is not typical, having an up to down quark ratio of two rather than a value of less than one as in the case of standard nuclei, such as Be (Cu) for which $u/d = 0.93$ (0.94). The theoretical calculations address this difference by calculating the nuclear cross sections using the actual numbers of protons and neutrons present in each case, but this alone does not fully compensate for the influence of the nuclear media surrounding interactions in targets other than hydrogen. As a result, values of $\langle k_T \rangle$ that yield agreement with nuclear data adjusted by $A^{\alpha-1}$ may not be fully appropriate for hydrogen. In particular, raising $\langle k_T \rangle$ by only 0.05 GeV/c drops the points in the lower two quadrants of Fig. 20 by enough (≈ 0.075 at 4.5 GeV/c) to approximately center these distributions on zero.

Figures 21 and 22 show the cross sections for inclusive π^0 production as functions of rapidity for pBe interactions at 530 and 800 GeV/c, for several intervals in p_T. The expected

peaking at a scattering angle near 90° in the center of mass ($y_{\rm cm} = 0$) develops slowly as a function of p_T. The shapes and normalizations of the data are in good agreement with the k_T-enhanced calculations.

Both theoretical and experimental uncertainties are reduced in the ratio of invariant cross sections for π^0 production at 800 and 530 GeV/c, allowing, in principle, a more sensitive test of the calculations. Figure 23 displays this ratio compared to conventional ($\langle k_T \rangle$=0) and k_T-enhanced NLO results using KKP fragmentation functions. The $\langle k_T \rangle$ values used here correspond to those used in Figs. 17 and 18. The energy dependence of the data is accommodated better by the k_T-enhanced theory. Similar conclusions are obtained for the hydrogen target data (not shown).

The results discussed in this section are not very sensitive to the reasonably well-known parton distribution functions [4] (quark distributions being of primary importance here). Methods similar to the ones described in this paper have been applied to analyze high-p_T hadron spectra in pp, pA, and AA collisions [71,72], and k_T effects have been found important for describing data on inclusive production of charged mesons.

B. η production

Cross sections for inclusive η production are tabulated in Tables VIII through XIII. Theoretical descriptions of η-meson production differ from the π^0 case primarily because of differences in the fragmentation of partons into the particles of interest. To investigate this aspect, we present η/π^0 relative production rates as functions of p_T and $y_{\rm cm}$ (for two p_T ranges) in Figs. 24 and 25 — the data average to a value of 0.45 ± 0.01 at 530 GeV/c, and 0.42 ± 0.01 at 800 GeV/c (for $3 < p_T < 8$ GeV/c).

V. SUMMARY

The invariant cross sections for π^0 and η production have been measured for pp and pBe collisions at 530 and 800 GeV/c as functions of p_T and $y_{\rm cm}$, over the kinematic range

$1 < p_T < 10$ GeV/c, and 1.5 units in rapidity. Results from k_T-enhanced NLO QCD calculations are in reasonable agreement with our measured π^0 cross sections. Employing the recent KKP fragmentation functions in the NLO QCD calculations was found to improve the description of the detailed shape of our π^0 cross sections (as a function of p_T) relative to theoretical results obtained using the earlier BKK fragmentation functions. The measured η/π^0 production ratios, which provide information about the relative fragmentation of partons into these mesons, are 0.45 ± 0.01 at 530 GeV/c and 0.42 ± 0.01 at 800 GeV/c, averaged over p_T and rapidity.

ACKNOWLEDGMENTS

We thank the U. S. Department of Energy, the National Science Foundation, including its Office of International Programs and the Universities Grants Commission of India, for their support of this research. The staff and management of Fermilab are thanked for their efforts in making available the beam and computing facilities that made this work possible. We are also pleased to acknowledge the contributions of our colleagues on Fermilab experiment E672. We acknowledge the contributions of the following colleagues during the upgrade and operation of the Meson West spectrometer: W. Dickerson, E. Pothier from Northeastern University; J. T. Anderson, E. Barsotti, Jr., H. Koecher, P. Madsen, D. Petravick, R. Tokarek, J. Tweed, D. Allspach, J. Urbin, R. L. Schmitt and the cryo crews from Fermi National Accelerator Laboratory; T. Haelen, C. Benson, L. Kuntz, and D. Ruggiero from the University of Rochester; the technical staffs of Michigan State University and Pennsylvania State University for the construction of the straw tubes and of the University of Pittsburgh for the silicon detectors. We would also like to thank the following commissioning run collaborators for their invaluable contributions to the hardware and software infrastructure of the original Meson West spectrometer: G. Alverson, G. Ballocchi, R. Benson, D. Berg, D. Brown, D. Carey, T. Chand, C. Chandlee, S. Easo, W. Faissler, G. Glass, I. Kourbanis, A. Lanaro, C. A. Nelson, Jr., D. Orris, B. M. Rajaram, K. Ruddick, A. Sinani-

dis, and G. Wu. We thank S. Catani, J.Ph. Guillet, B. Kniehl, J. Owens, G. Sterman, and W. Vogelsang for many helpful discussions and for providing us with their QCD calculations.

REFERENCES

[1] W. M. Geist *et al.*, Phys. Rep. **197**, 263 (1990).

[2] N. A. McCubbin, Rep. Prog. Phys. **44**, 65 (1981).

[3] F. Aversa *et al.*, Nucl. Phys. **B327**, 105 (1989).

[4] L. Apanasevich *et al.*, Phys. Rev. Lett. **81**, 2642 (1998).

[5] L. Apanasevich *et al.*, Phys. Rev. **D59**, 074007 (1999).

[6] J. Huston *et al.*, Phys. Rev. **D51**, 6139 (1995).

[7] P. Aurenche *et al.*, Eur. Phys. J. **C9**, 107 (1999).

[8] P. Aurenche *et al.*, Eur. Phys. J. **C13**, 347 (2000).

[9] k_T denotes the magnitude of the effective transverse momentum vector, $\vec{k}_T$, of each of the two colliding partons.

[10] J. Breitweg *et al.*, Phys. Lett. **472B**, 175 (2000).

[11] J. Breitweg *et al.*, Phys. Lett. **511B**, 19 (2001).

[12] M. Fontannaz, J. P. Guillet, and G. Heinrich, Eur. Phys. J. **C21**, 303 (2001).

[13] M. Fontannaz, J. P. Guillet, and G. Heinrich, Eur. Phys. J. **C22**, 303 (2001).

[14] A. Zembrzuski and M. Krawczyk, Phys. Rev. **D64**, 114017 (2001).

[15] J. F. Owens, Phys. Rev. **D65**, 034011 (2002).

[16] G. Alverson *et al.*, Phys. Rev. **D48**, 5 (1993).

[17] G. Alverson *et al.*, Phys. Rev. **D45**, 3899 (1992).

[18] G. Alverson *et al.*, Phys. Rev. Lett. **68**, 2584 (1992).

[19] G. Alverson *et al.*, Phys. Rev. **D49**, 3106 (1994).

[20] L. Apanasevich *et al.*, Phys. Rev. **D56**, 1391 (1997).

[21] D. Striley, Ph.D. thesis, University of Missouri at Columbia, 1996.

[22] I. Kourbanis, Ph.D. thesis, Northeastern University, 1989.

[23] D. Allspach *et al.*, in *Advances in Cyrogenic Engineering*, edited by R. W. Fast (Plenum Press, New York, 1991), Vol. 37, p. 1495.

[24] E. Engels, Jr. *et al.*, Nucl. Instrum. Methods Phys. Res. **A279**, 272 (1989).

[25] C. Bromberg *et al.*, Nucl. Instrum. Methods Phys. Res. **A307**, 292 (1991).

[26] These hybrid planes were installed after the commissioning run to provide improved vertex resolution.

[27] F. Lobkowicz *et al.*, Nucl. Instrum. Methods Phys. Res. **A235**, 332 (1985).

[28] L. Apanasevich *et al.*, Nucl. Instrum. Methods Phys. Res. **A417**, 50 (1998).

[29] G. Drake *et al.*, Nucl. Instrum. Methods Phys. Res. **A269**, 68 (1988).

[30] C. Lirakis, in *Proceedings of the First Annual Conference on Electronics for Future Colliders, May 22-23, 1991* (Le Croy Corp., Chestnut Ridge, New York, 1991), p. 35.

[31] Charles Benson, M.S. thesis, University of Rochester, 1989.

[32] A. Gribushin *et al.*, Phys. Rev. **D53**, 4723 (1996).

[33] A. Gribushin *et al.*, Phys. Rev. **D62**, 012001 (2000).

[34] V. Koreshev *et al.*, Phys. Rev. Lett. **77**, 4294 (1996).

[35] R. Jesik *et al.*, Phys. Rev. Lett. **74**, 495 (1995).

[36] The fiducial volume of the hydrogen target was defined to exclude interactions with the mylar walls of the target flask.

[37] Binned in p_T, rapidity, and vertex position, simulated π^0 and η mesons were allowed to decay isotropically to two photons. Photon pairs that satisfied the energy asymmetry requirement (as defined in the text) were projected to the EMLAC, and selected on the basis of the standard fiducial acceptance criteria.

[38] The calculations of invariant mass and p_T assumed that the photons originated from the reconstructed interaction vertex.

[39] D. E. Groom *et al.*, Eur. Phys. J. **C15**, 1 (2000).

[40] The response of each trigger group was evaluated as a function of p_T reconstructed within the group, using data samples that were not biased in that region. The sample used for obtaining the efficiency of the SINGLE LOCAL HI trigger was based on information from octants that fired the SINGLE LOCAL LO trigger. The sample used to evaluate the response of the SINGLE LOCAL LO trigger used information from the octants opposite those that satisfied the SINGLE LOCAL HI trigger. In the case of the PRETRIGGER HI,

octants located opposite those that satisfied the SINGLE LOCAL HI trigger were used to measure the trigger efficiency for the trigger groups comprised of the inner and outer R channels in each octant.

[41] L. Sorrell, Ph.D. thesis, Michigan State University, 1995.

[42] G. Osborne, Ph.D. thesis, University of Rochester, 1996.

[43] F. Carminati *et al.*, GEANT: Detector Description and Simulation Tool, CERN Program Library Long Writeup W5013, 1993.

[44] This is in contrast to the analysis of data from the commissioning run where we used just empirical parameterizations of the electromagnetic showers in simulating the EMLAC response.

[45] Fermilab Computing Department, CPS Software User's Guide, FNAL GA0009 (1993).

[46] G. Marchesini *et al.*, Comput. Phys. Commun. **67**, 465 (1992), HERWIG v5.6.

[47] T. Sjöstrand, PYTHIA 5.6 and JETSET 7.3 Physics and Manual, CERN-TH.6488/92, 1992.

[48] L. Apanasevich *et al.*, (in preparation).

[49] M. Bonesini *et al.*, Z. Phys. C **37**, 39 (1987).

[50] G. Donaldson *et al.*, Phys. Rev. Lett. **40**, 917 (1978).

[51] G. D. Lafferty and T. R. Wyatt, Nucl. Instrum. Methods Phys. Res. **A355**, 541 (1995).

[52] H. L. Lai *et al.*, Phys. Rev. **D55**, 1280 (1997).

[53] J. Binnewies, B. A. Kniehl, and G. Kramer, Phys. Rev. **D52**, 4947 (1995).

[54] B. A. Kniehl, G. Kramer, and B. Pötter, Nucl. Phys. **B582**, 514 (2000).

[55] R. P. Feynman, R. D. Field, and G. C. Fox, Phys. Rev. **D18**, 3320 (1978).

[56] M. Fontannaz and D. Schiff, Nucl. Phys. **B132**, 457 (1978).

[57] A. P. Contogouris *et al.*, Nucl. Phys. **B179**, 461 (1981).

[58] A. P. Contogouris *et al.*, Phys. Rev. **D32**, 1134 (1985).

[59] J. Collins and D. Soper, Nucl. Phys. **B193**, 381 (1981); **B213**, 545(E) (1983); J. Collins, D. Soper, G. Sterman, Phys. Lett. **109B**, 388 (1982).

[60] S. Catani *et al.*, JHEP **03**, 025 (1999).

[61] S. Catani, M. L. Mangano, and P. Nason, JHEP **07**, 024 (1998).

[62] H.-L. Lai and H.-N. Li, Phys. Rev. **D58**, 114020 (1998).

[63] E. Laenen, G. Sterman, and W. Vogelsang, Phys. Rev. Lett. **84**, 4296 (2000).

[64] E. Laenen, G. Oderda, and G. Sterman, Phys. Lett. **B438**, 173 (1998).

[65] N. Kidonakis, G. Oderda, and G. Sterman, hep-ph/9805279 (1998).

[66] N. Kidonakis, G. Oderda, and G. Sterman, Nucl. Phys. **B525**, 299 (1998).

[67] C. E. Fink, hep-ph/0105276 (2001).

[68] J. F. Owens, Rev. Mod. Phys. **59**, 465 (1987).

[69] A. G. Clark *et al.*, Nucl. Phys. **B160**, 397 (1979).

[70] A. L. S. Angelis *et al.*, Phys. Lett. **97B**, 163 (1980).

[71] X.-N. Wang, Nucl. Phys. **A661**, 609 (1999).

[72] Y. Zhang *et al.*, Phys. Rev. **C65**, 034903 (2002).

FIG. 1. Plan view of the Fermilab Meson West spectrometer, as configured for the 1991-92 fixed target run.

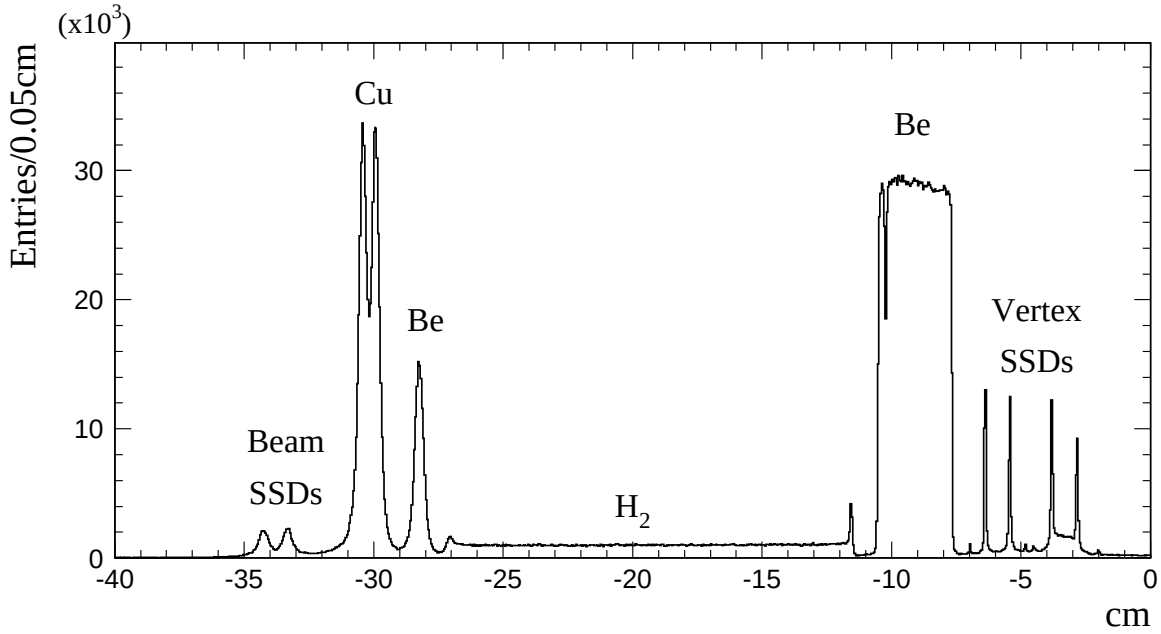

FIG. 2. Distribution of the reconstructed vertex position (along Z) for the combined 530 and 800 GeV/c data. The clearly-resolved individual target elements are, from the left: two copper foils, the liquid hydrogen target (a mylar flask enclosed between two thin Be windows), followed by the main beryllium target. The two silicon strip detectors (SSDs) immediately upstream and four downstream of the target can also be easily distinguished.

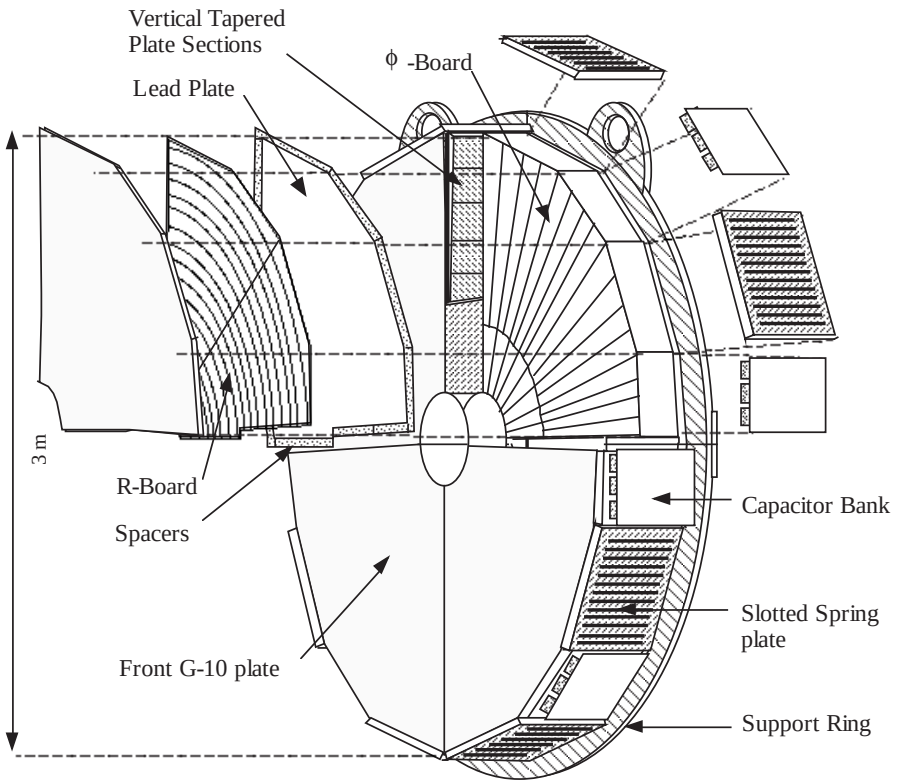

FIG. 3. The physical layout of the liquid argon electromagnetic calorimeter (EMLAC).

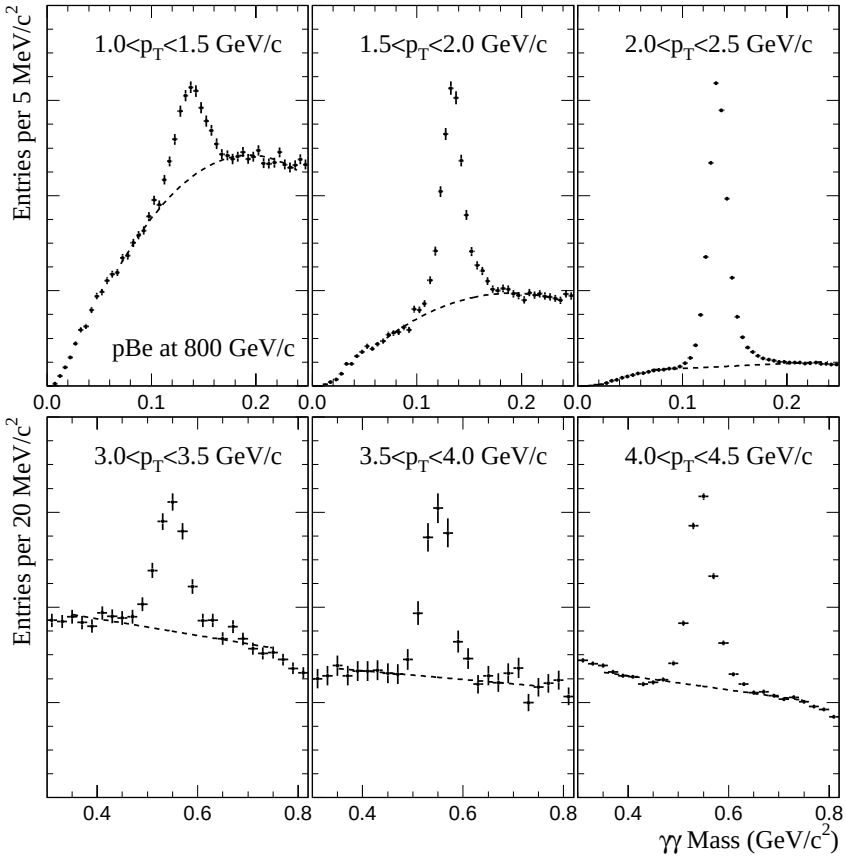

FIG. 4. $\gamma\gamma$ mass distributions in the region of the π^0 (top row) and the η (bottom row) mesons from pBe interactions at 800 GeV/c, for several ranges of $\gamma\gamma$ p_T-values.

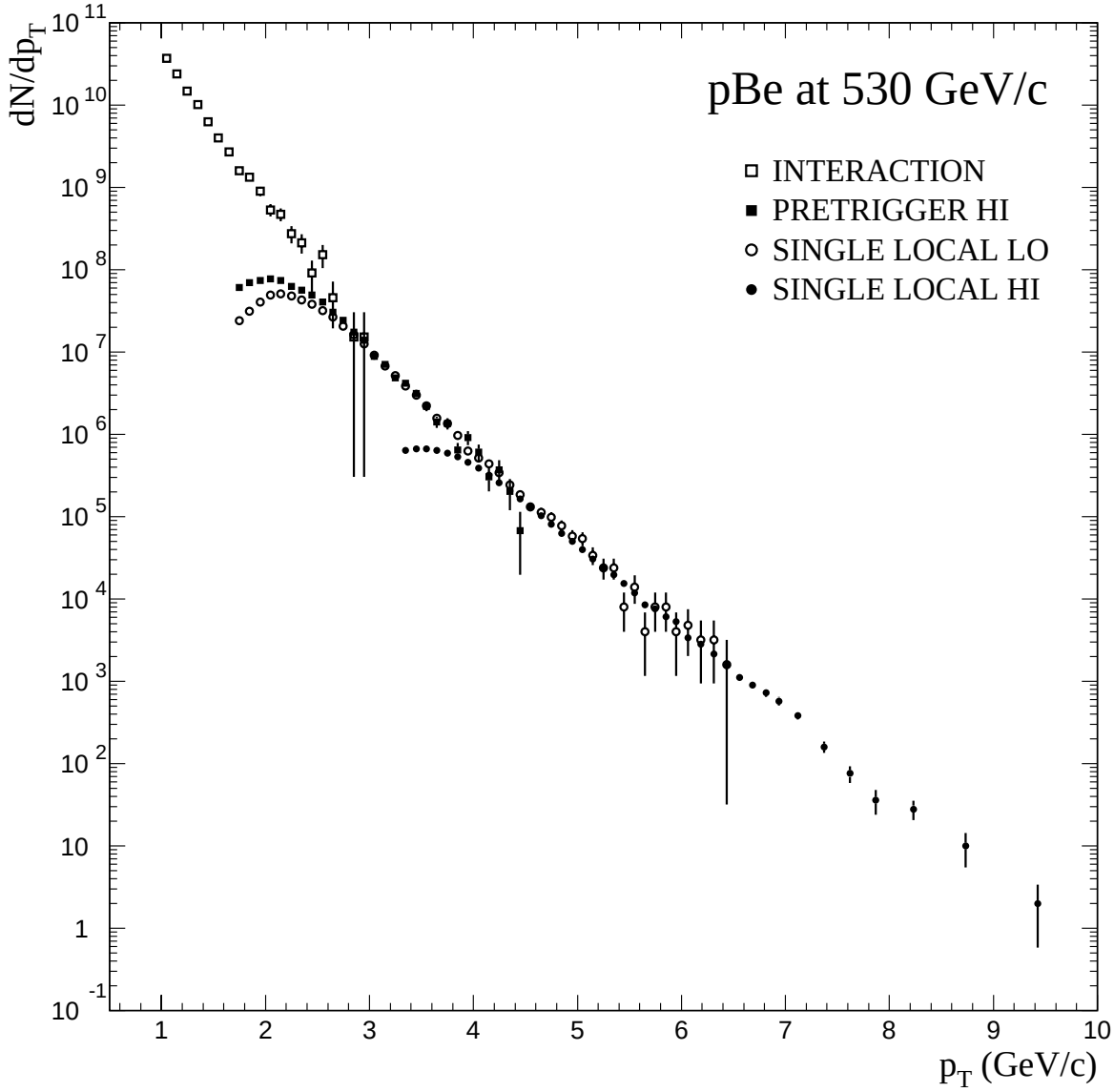

FIG. 5. p_T spectra of π^0 candidates from 530 GeV/c proton interactions on Be, selected via several different triggers implemented with significantly different prescale factors. The data have only been corrected for trigger prescale factors.

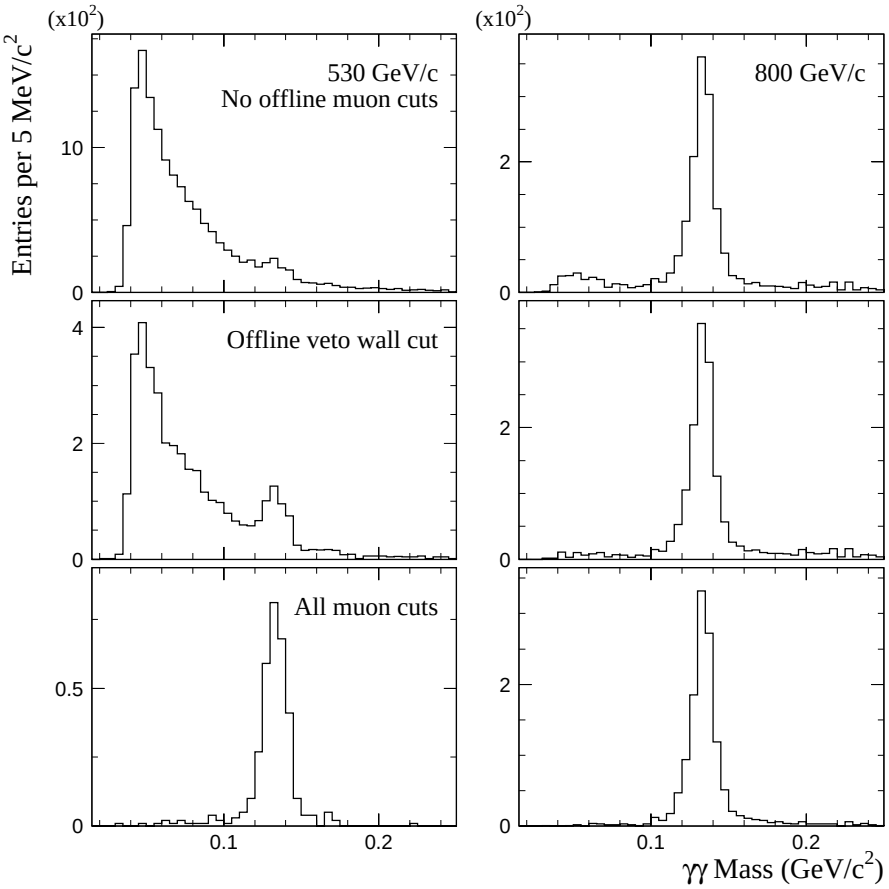

FIG. 6. Effect of beam halo muon induced shower discriminators on the $\gamma\gamma$ invariant mass distribution in the π^0-mass region, for $\gamma\gamma$ pairs with $p_T > 7$ GeV/c in the 530 GeV/c data (left) and in the 800 GeV/c data (right).

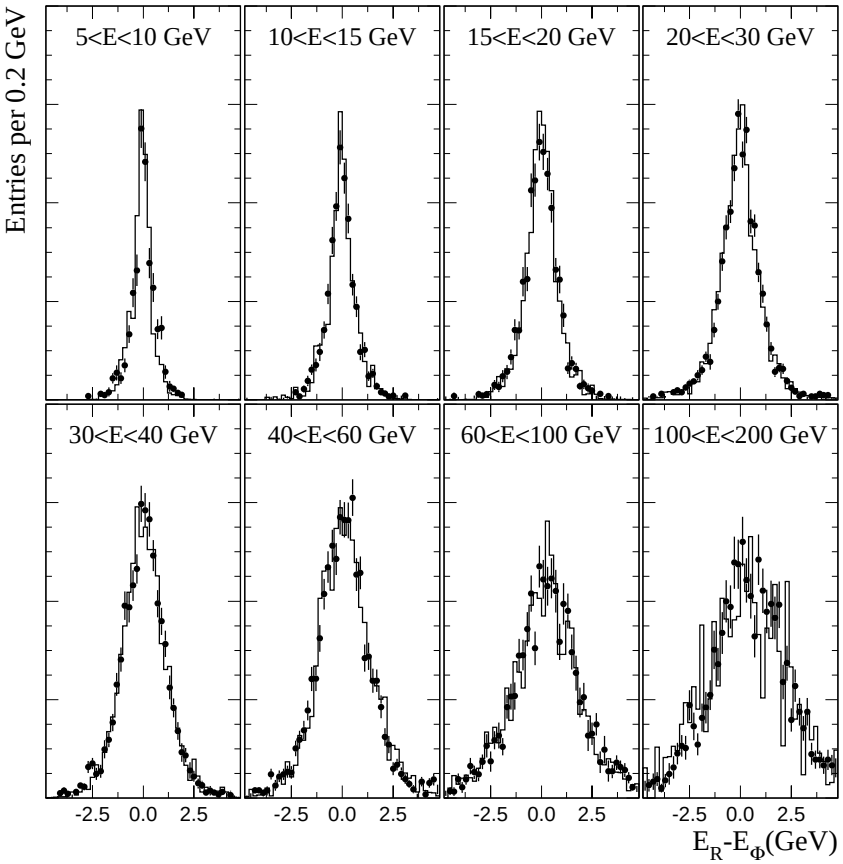

FIG. 7. Comparisons of distributions in photon $E_R - E_\Phi$, for eight photon-energy bins, between data (histogram) and the Monte Carlo simulation (points) for the 530 GeV/c sample. The photons are from π^0 candidates with $p_T > 3.5$ GeV/c.

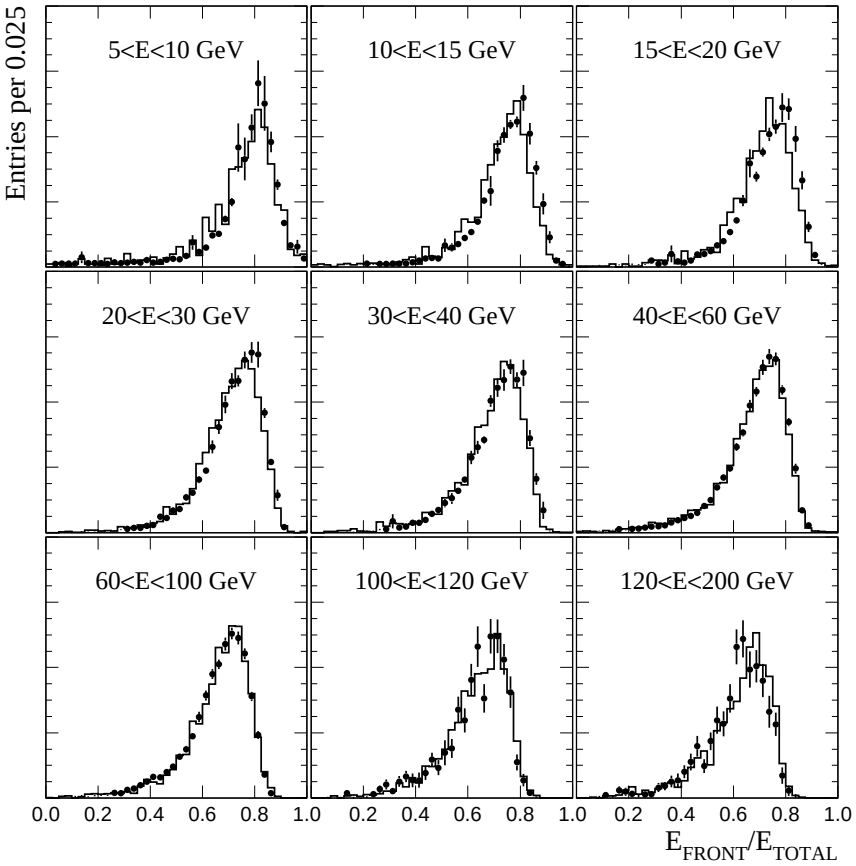

FIG. 8. Comparison of the photon $E_{\mathrm{FRONT}}/E_{\mathrm{TOTAL}}$ distributions, in nine photon-energy bins, between data (histogram) and the Monte Carlo simulation (points), for the 800 GeV/c sample. The photons originated from decays of π^0 candidates with $p_T > 3.5$ GeV/c.

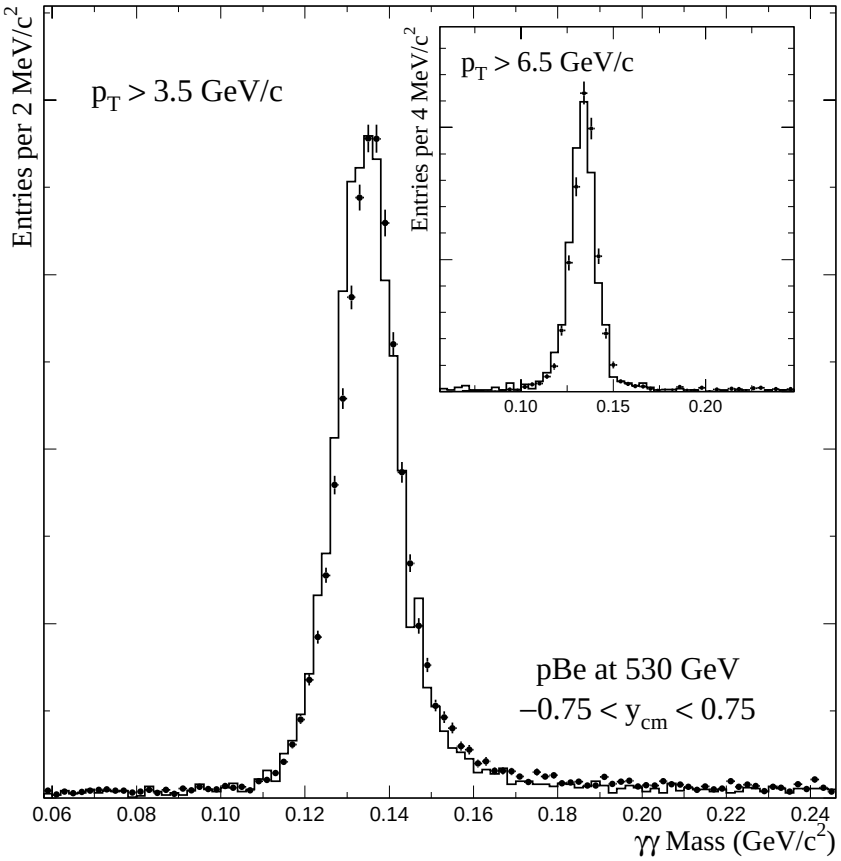

FIG. 9. $\gamma\gamma$ mass distributions in the π^0 signal region in the 530 GeV/c data (histogram) compared to Monte Carlo simulations (points) for two requirements on minimum p_T.

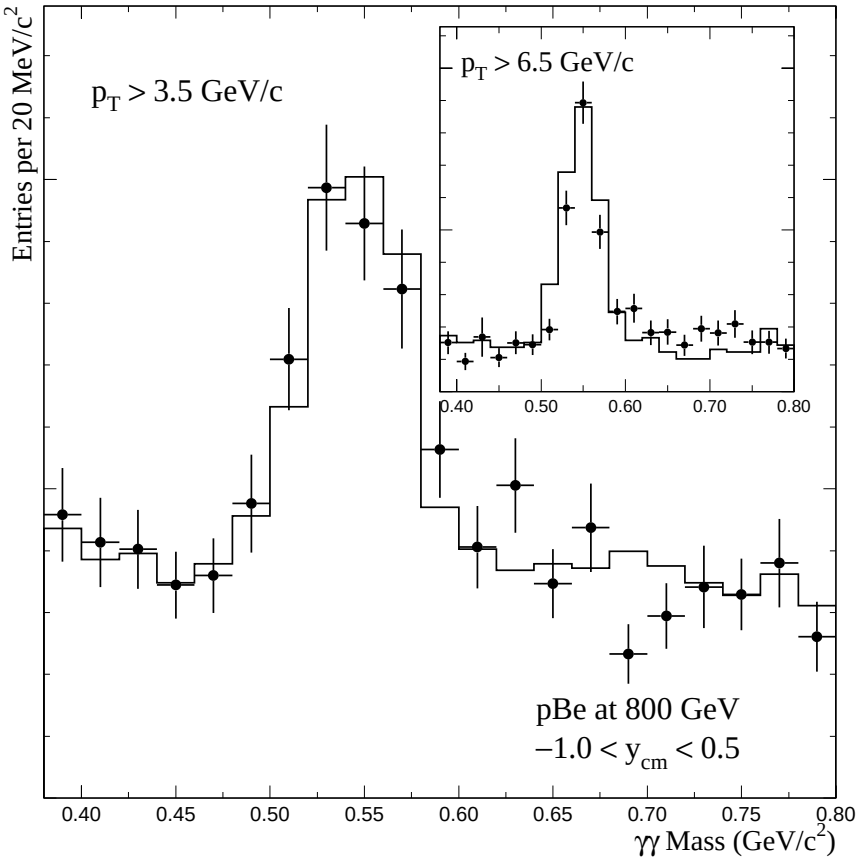

FIG. 10. $\gamma\gamma$ mass distributions in the η signal region in the 800 GeV/c data (histogram) compared to Monte Carlo simulations (points) for two requirements on minimum p_T.

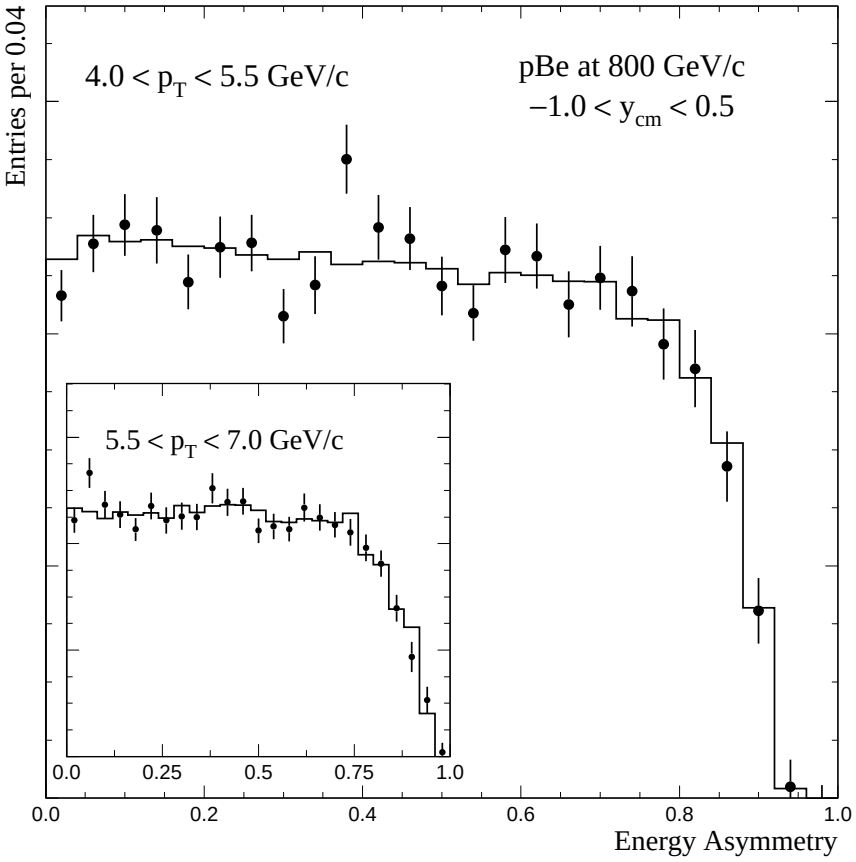

FIG. 11. Comparison of $\gamma\gamma$ energy asymmetry distribution for π^0 mesons in the data (histogram) and the Monte Carlo (points) for 800 GeV/c pBe interactions, for the p_T intervals $4.0 < p_T < 5.5$ GeV/c and $5.5 < p_T < 7.0$ GeV/c. These distributions have been corrected for contributions from background sources.

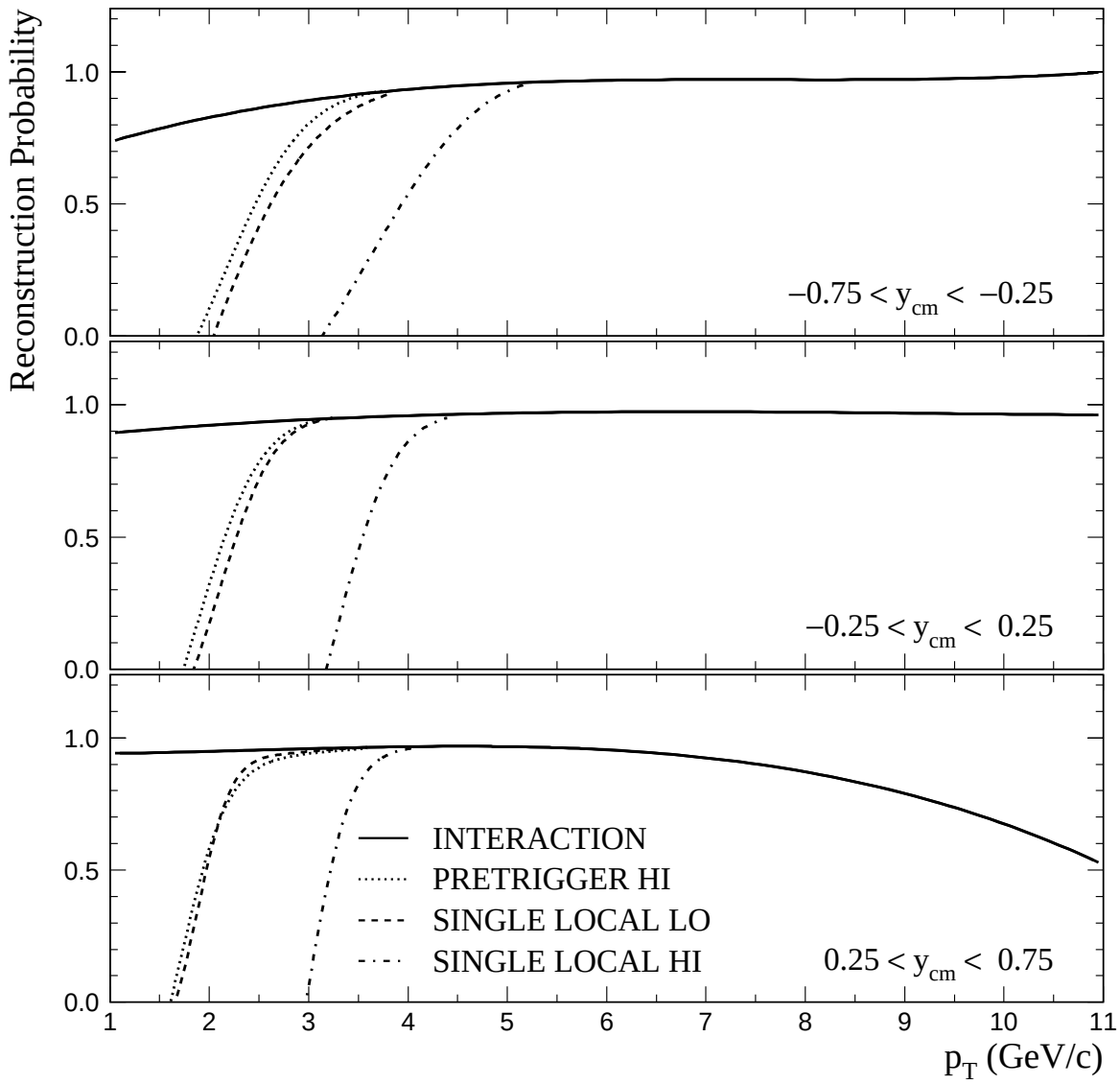

FIG. 12. Probability for accepting a π^0 candidate (in the 530 GeV/c Monte Carlo sample) as a function of p_T for three rapidity intervals and different triggers. This probability reflects the losses due to the reconstruction algorithm, the $E_{\rm FRONT}/E_{\rm TOTAL}$ criterion, and the individual trigger requirements (see text for details).

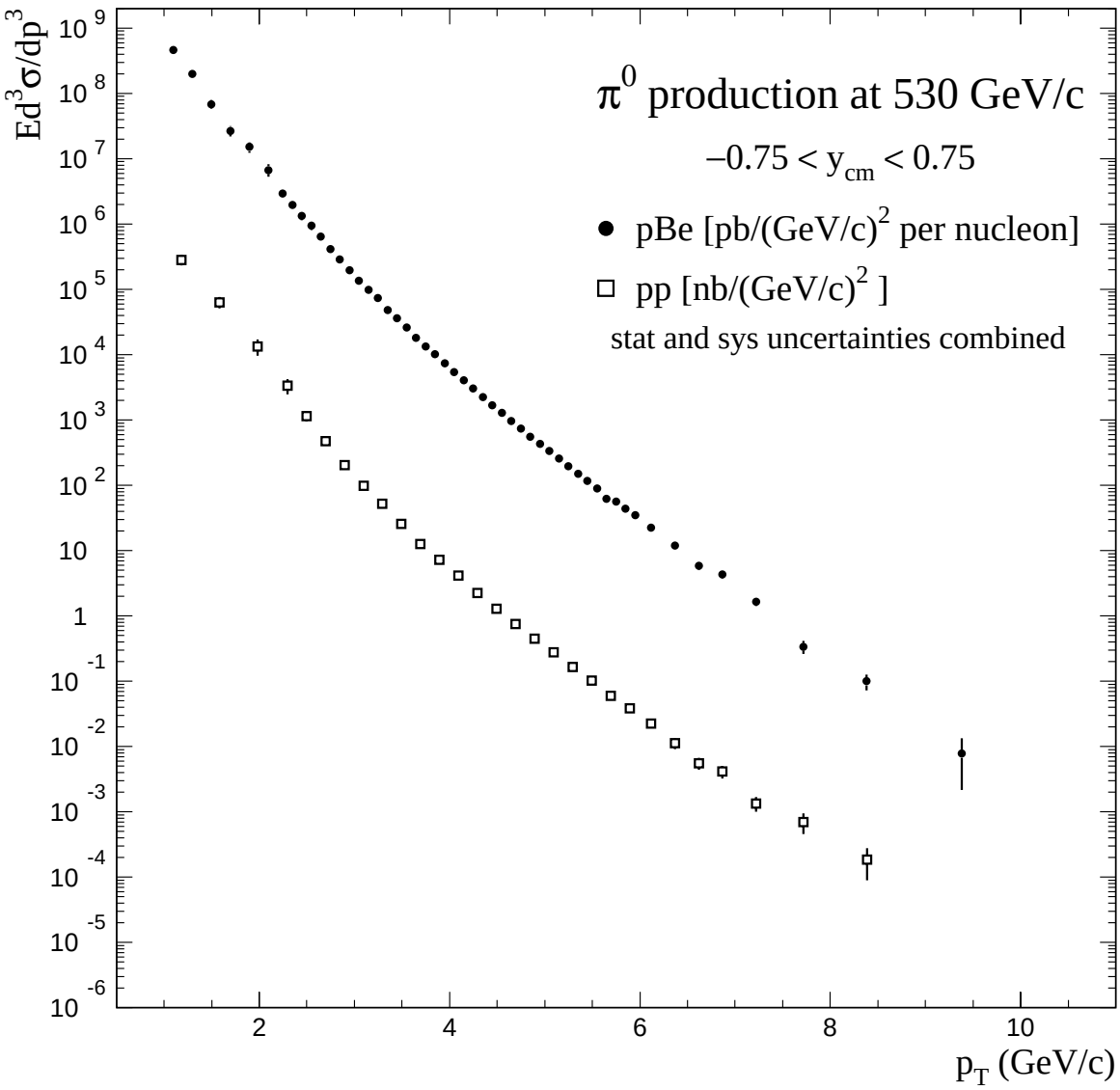

FIG. 13. Invariant differential cross sections (per nucleon) for π^0 production as a function of π^0 p_T in pp and pBe interactions at 530 GeV/c. Cross sections have been averaged over the full rapidity range, $-0.75 \leq y_{\rm cm} \leq 0.75$. The error bars have experimental statistical and systematic uncertainties added in quadrature.

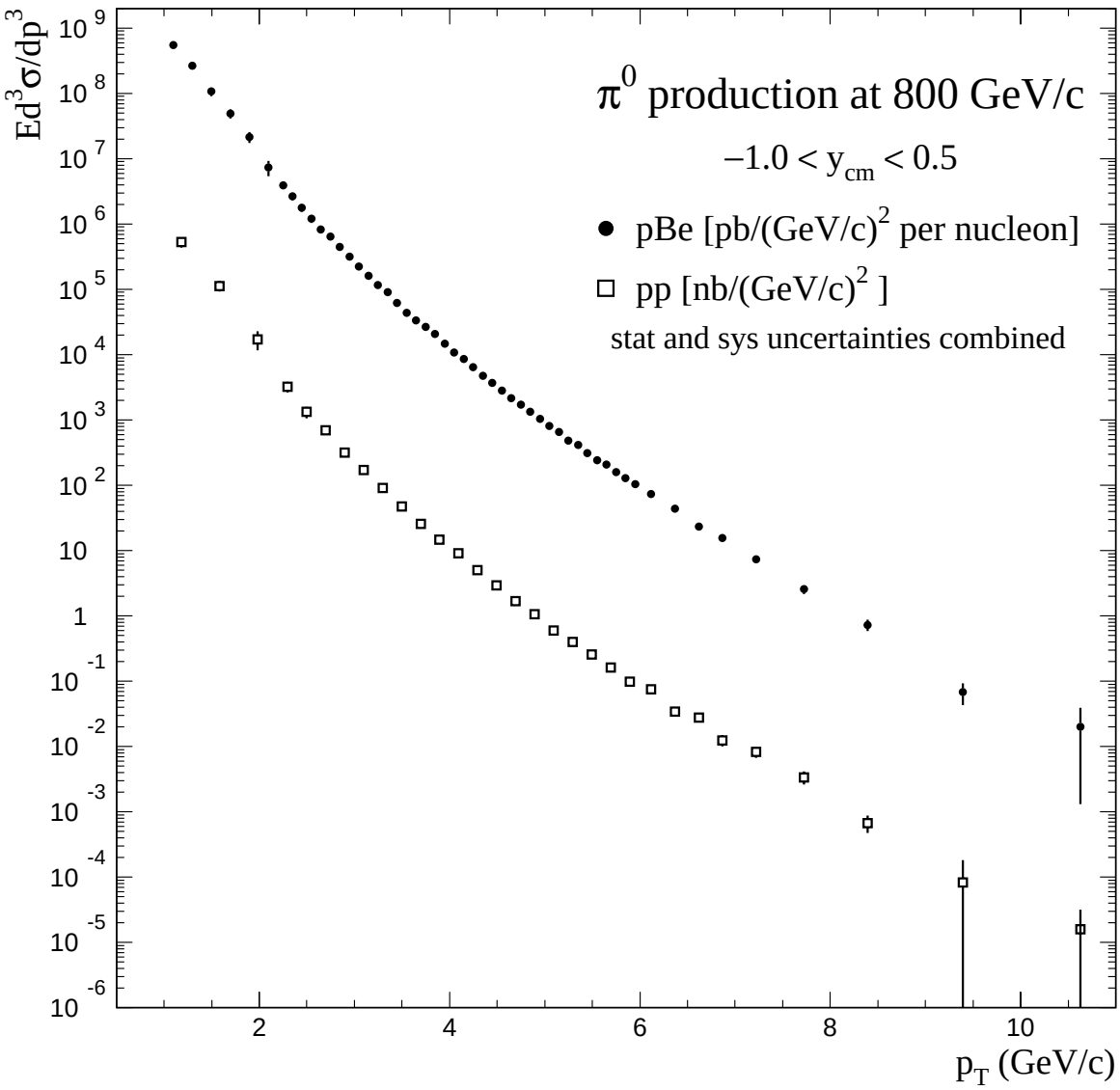

FIG. 14. Invariant differential cross sections (per nucleon) for π^0 production as a function of π^0 p_T in pp and pBe interactions at 800 GeV/c. Cross sections have been averaged over the full rapidity range, $-1.0 \leq y_{\rm cm} \leq 0.5$. The error bars have experimental statistical and systematic uncertainties added in quadrature.

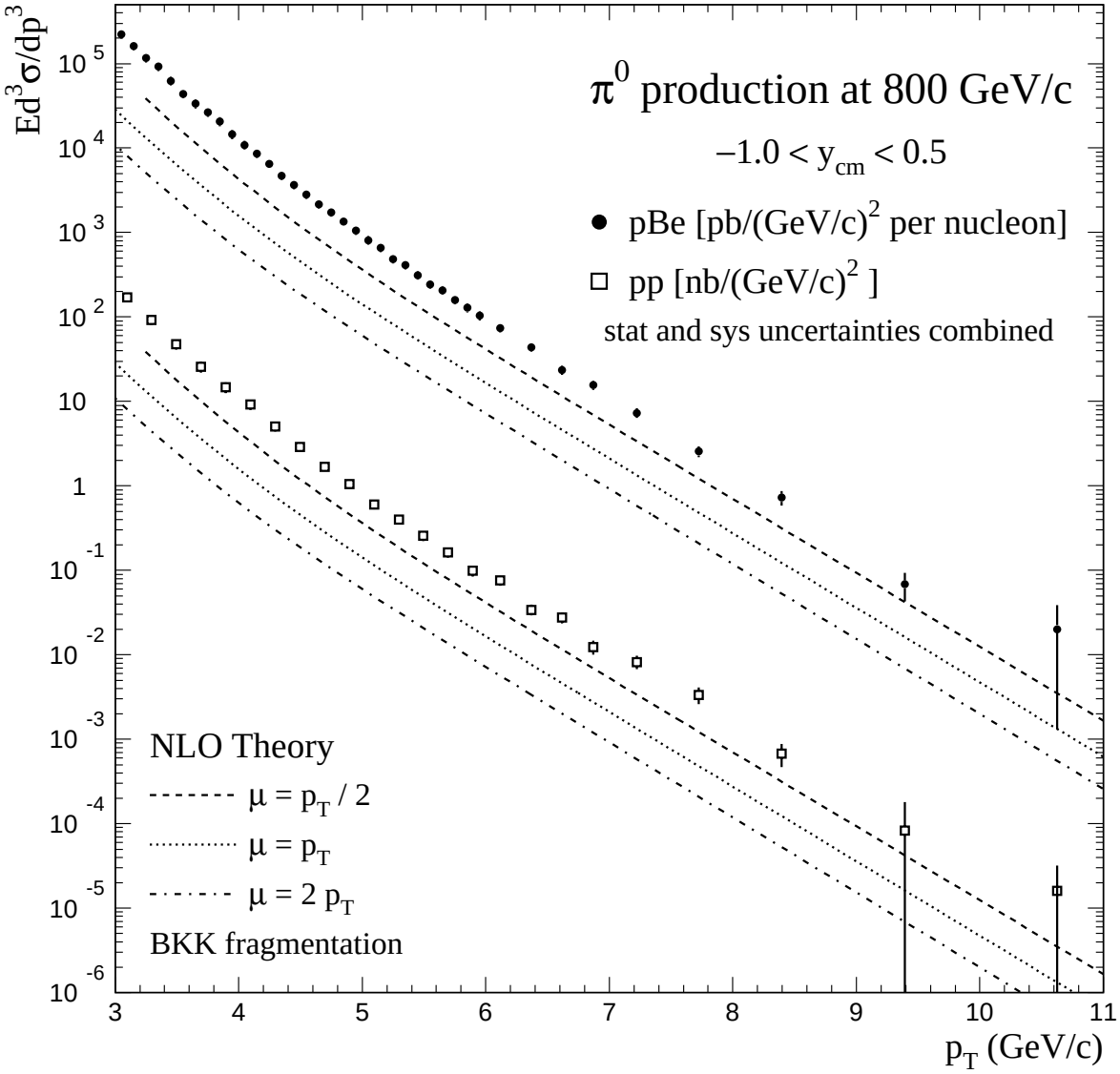

FIG. 15. Invariant differential cross sections (per nucleon) for π^0 production as a function of π^0 p_T in pBe and pp interactions at 800 GeV/c compared to NLO PQCD calculations, with scale choices of $\mu = p_T/2$, p_T, and $2p_T$. The error bars have experimental statistical and systematic uncertainties added in quadrature.

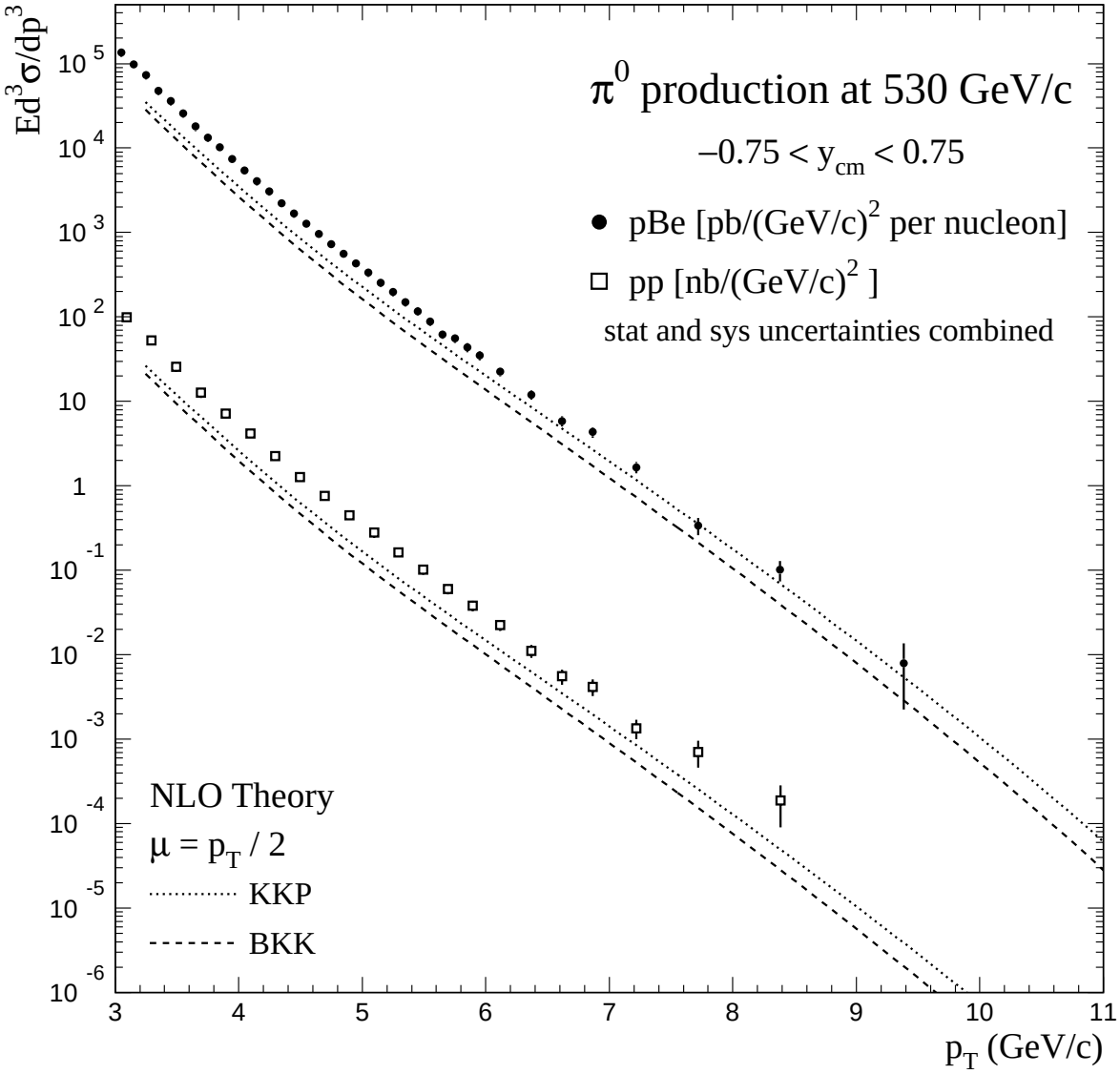

FIG. 16. Invariant differential cross sections (per nucleon) for π^0 production as a function of π^0 p_T in pBe and pp interactions at 530 GeV/c compared to NLO PQCD calculations, with scale $\mu = p_T/2$ and BKK and KKP fragmentation functions. The error bars have experimental statistical and systematic uncertainties added in quadrature.

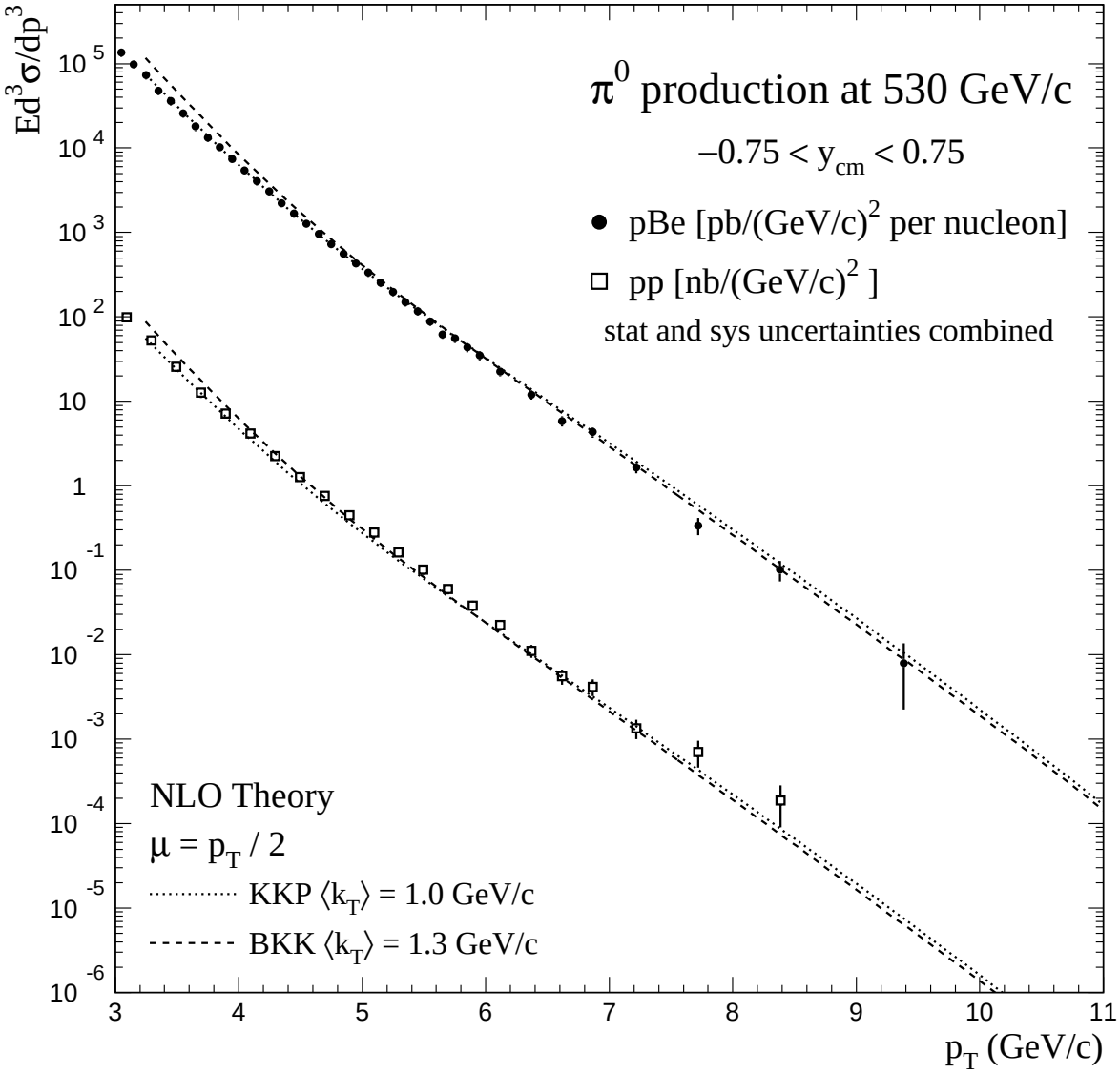

FIG. 17. Invariant differential cross sections (per nucleon) for π^0 production as a function of π^0 p_T in pBe and pp interactions at 530 GeV/c compared to k_T-enhanced NLO PQCD calculations with scale $\mu = p_T/2$. Comparisons are shown for both BKK and KKP fragmentation functions. The error bars have experimental statistical and systematic uncertainties added in quadrature.

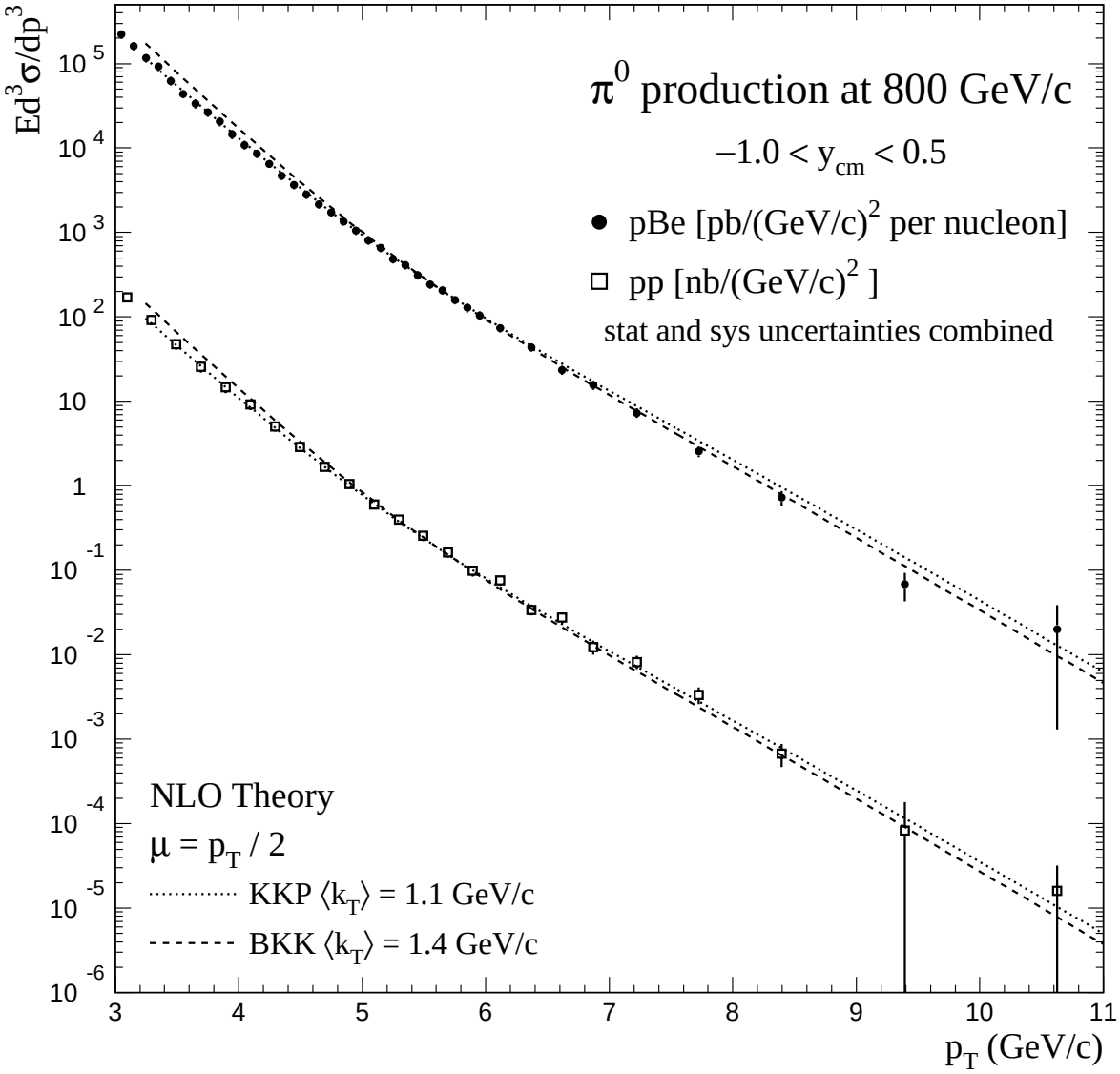

FIG. 18. Invariant differential cross sections (per nucleon) for π^0 production as a function of π^0 p_T in pBe and pp interactions at 800 GeV/c compared to k_T-enhanced NLO PQCD calculations, with scale $\mu = p_T/2$. Comparisons are shown for both BKK and KKP fragmentation functions. The error bars have experimental statistical and systematic uncertainties added in quadrature.

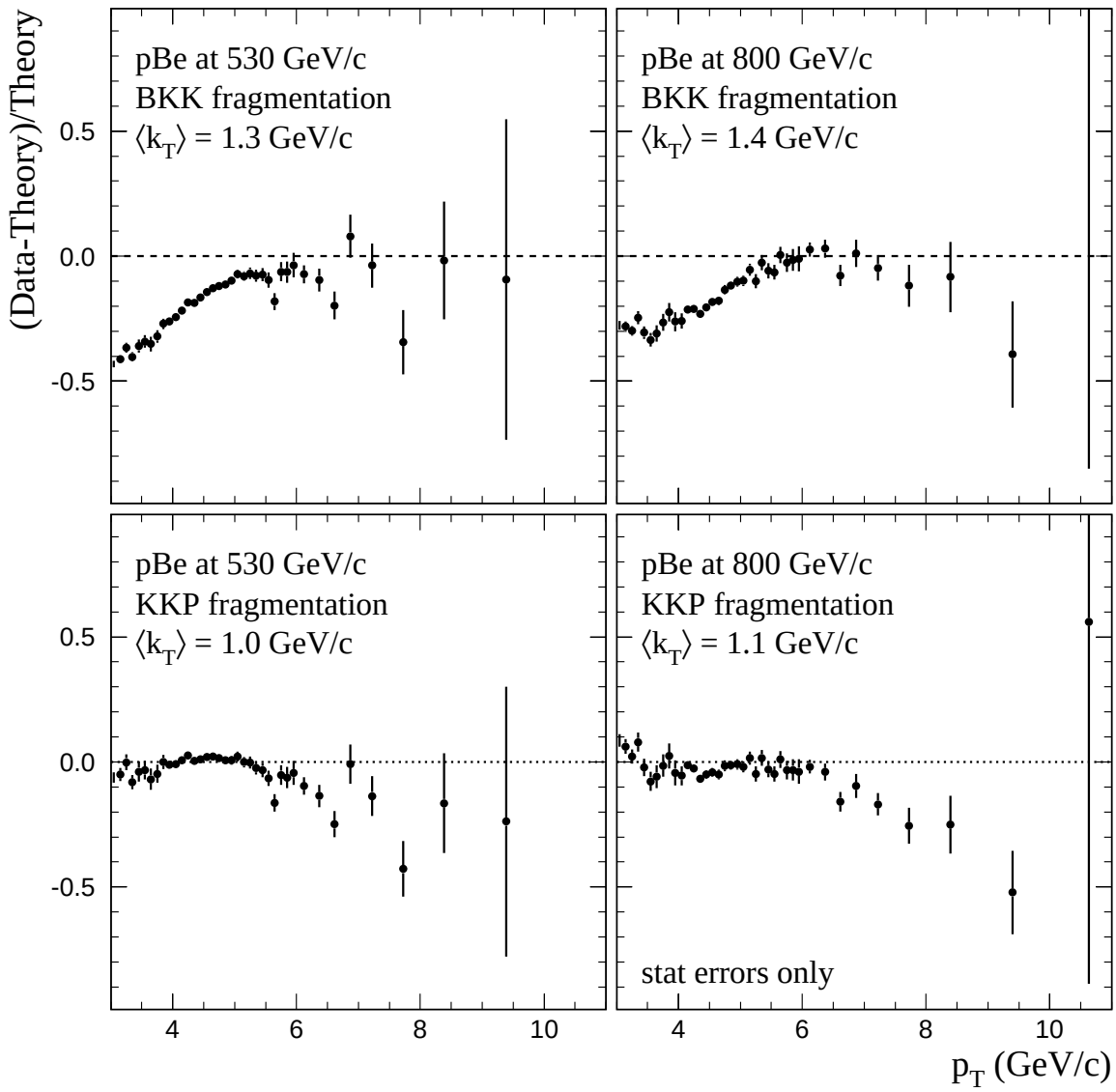

FIG. 19. Fractional difference between data and k_T-enhanced NLO PQCD calculations for π^0 production in pBe interactions at 530 and 800 GeV/c as a function of π^0 p_T. The error bars represent only statistical contributions.

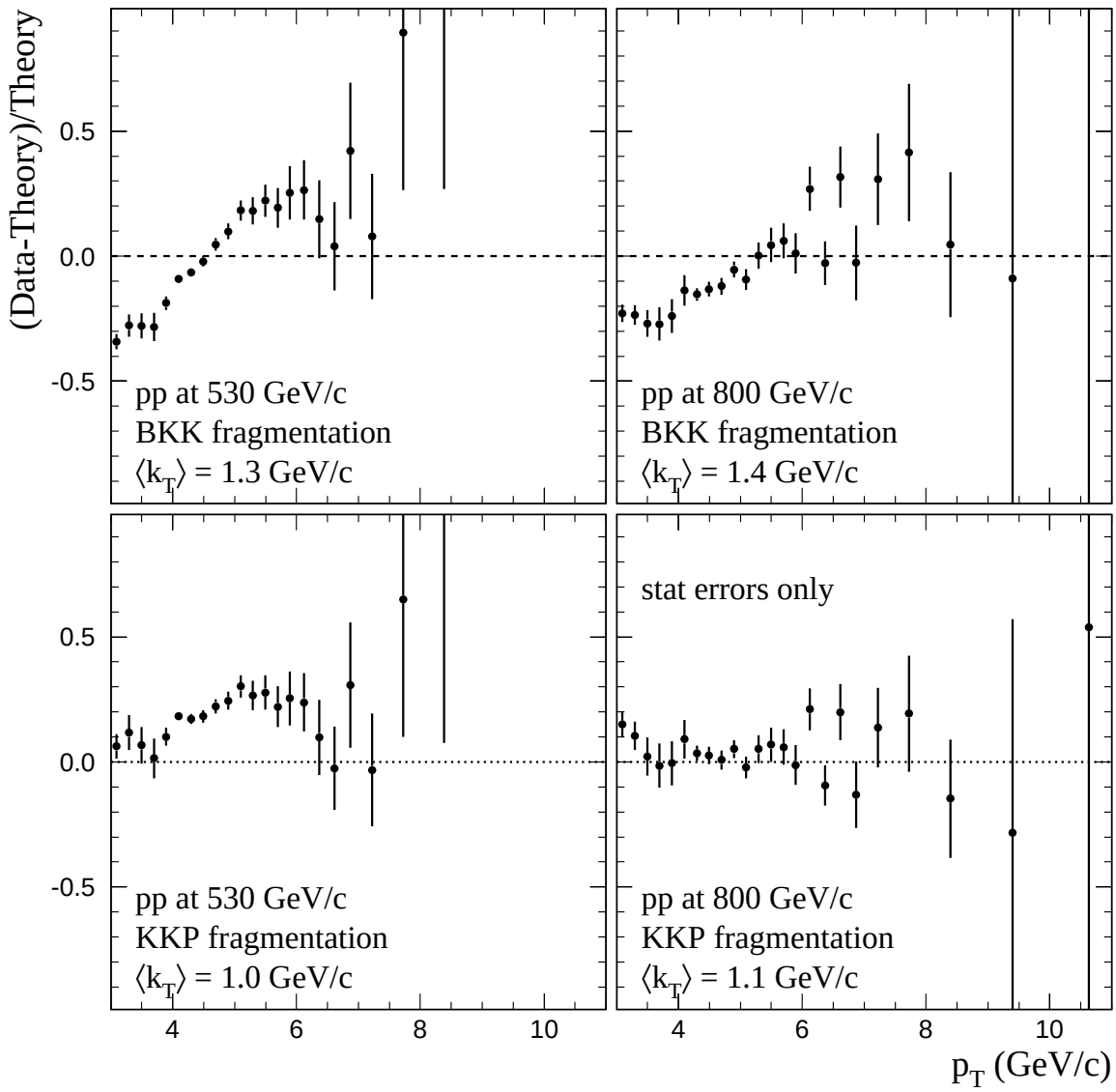

FIG. 20. Fractional difference between data and k_T-enhanced NLO PQCD results for π^0 production in pp interactions at 530 and 800 GeV/c as a function of π^0 p_T. The error bars represent only statistical contributions.

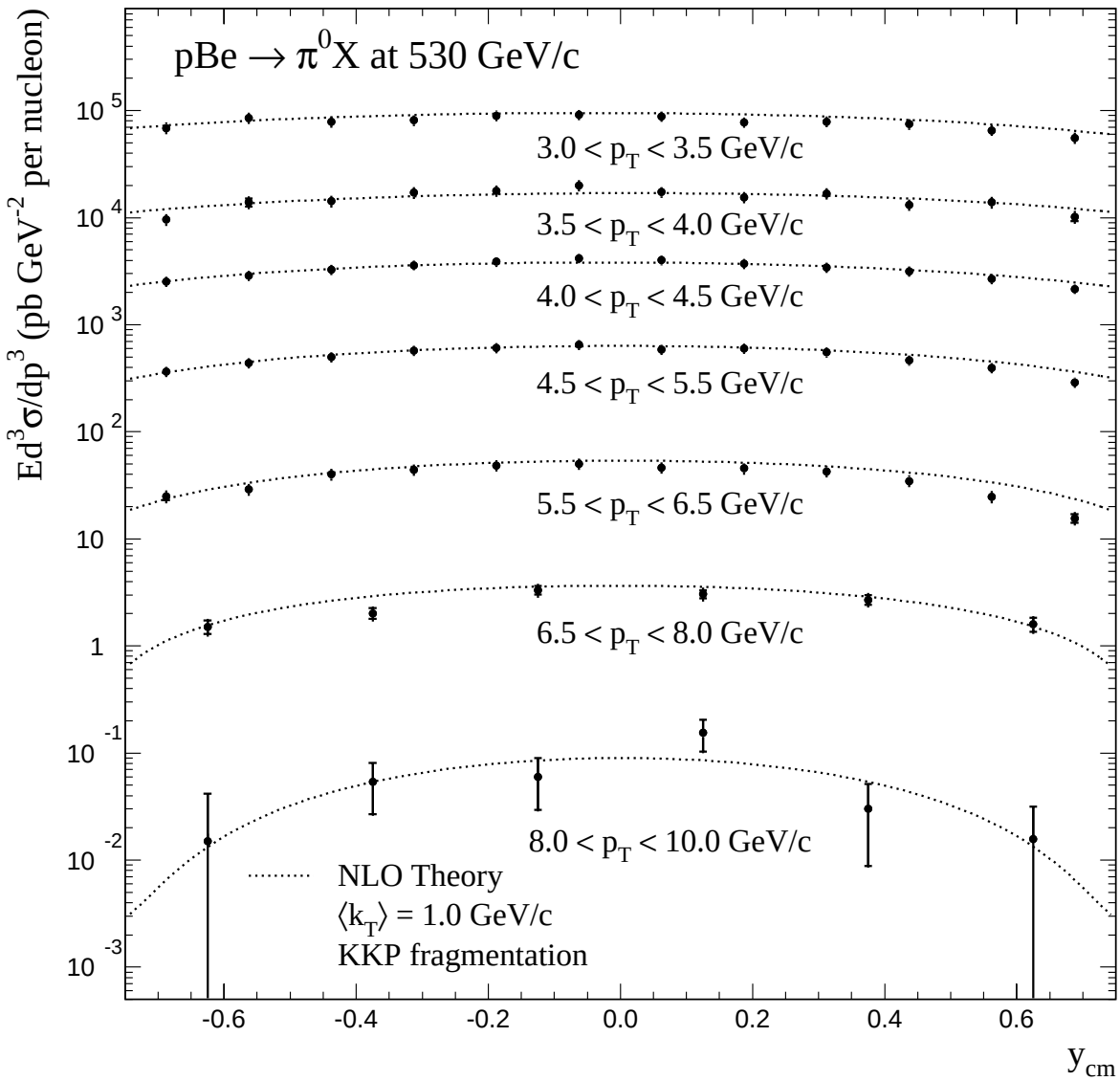

FIG. 21. Invariant cross sections per nucleon for π^0 production in pBe interactions at 530 GeV/c. Cross sections are shown versus $y_{\rm cm}$ for several intervals in p_T. The curves represent the k_T-enhanced NLO QCD calculations for $\langle k_T \rangle$=1.0 GeV/c and $\mu = p_T/2$, using KKP fragmentation functions. The error bars have experimental statistical and systematic uncertainties added in quadrature.

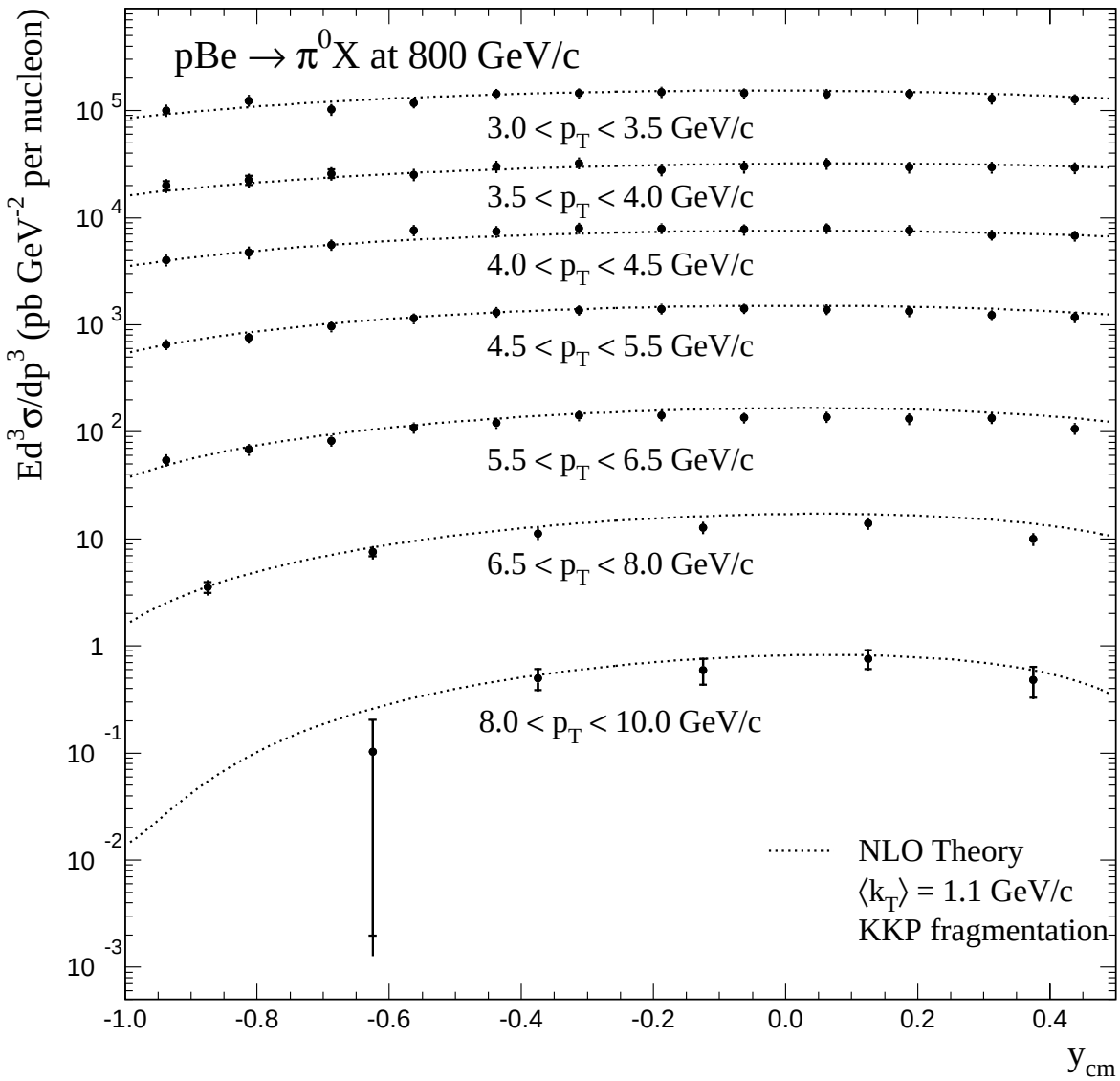

FIG. 22. Invariant cross section per nucleon for π^0 production in pBe interactions at 800 GeV/c. Cross sections are shown versus $y_{\rm cm}$ for several intervals in p_T. The curves represent the k_T-enhanced NLO QCD calculations for $\langle k_T \rangle$=1.1 GeV/c and $\mu = p_T/2$, using KKP fragmentation functions. The error bars have experimental statistical and systematic uncertainties added in quadrature.

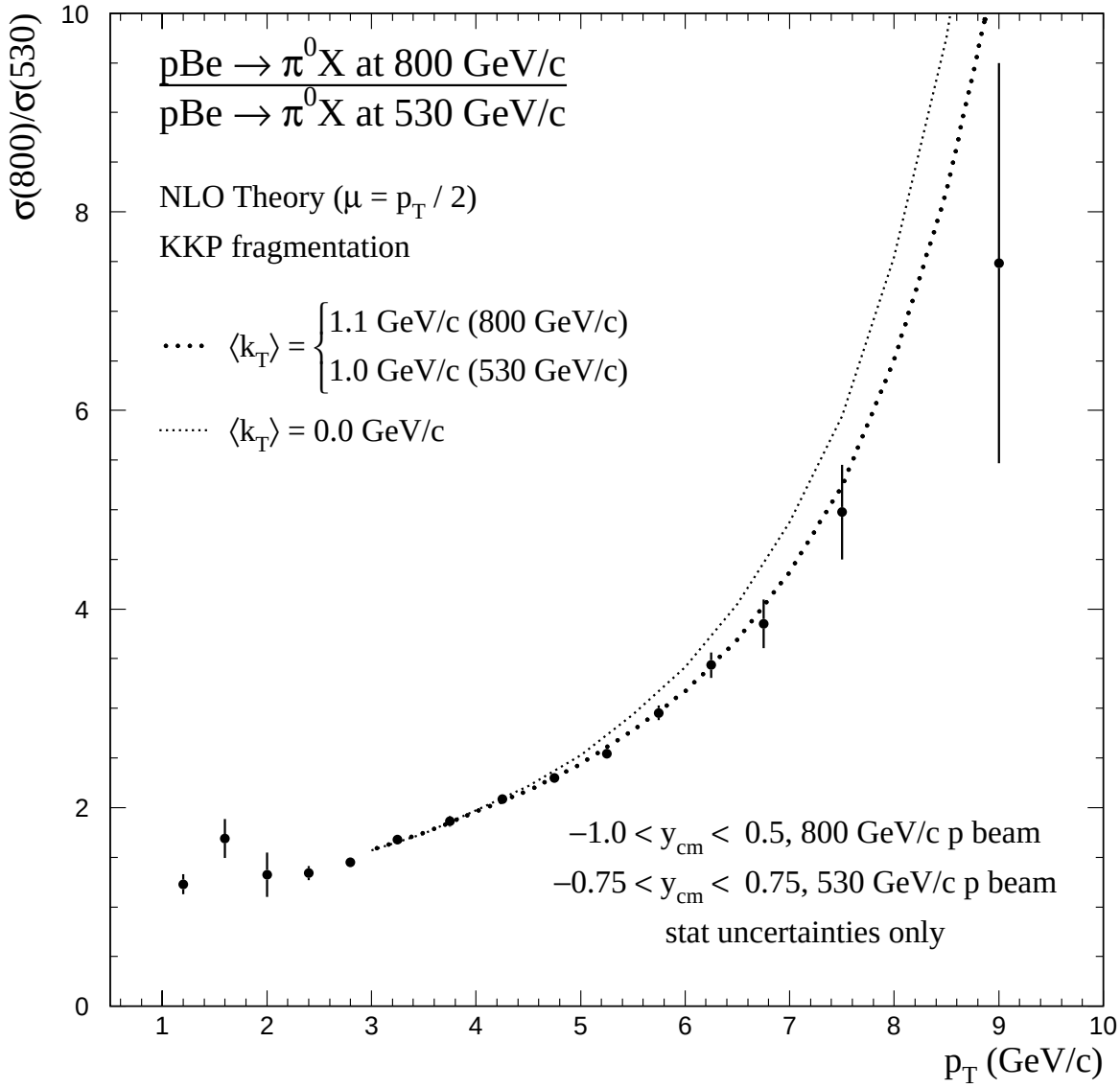

FIG. 23. Ratio of invariant cross sections for π^0 production in pBe interactions at 800 and 530 GeV/c as a function of π^0 p_T, compared to conventional and k_T-enhanced NLO QCD results using KKP fragmentation functions. The error bars reflect only the statistical uncertainties.

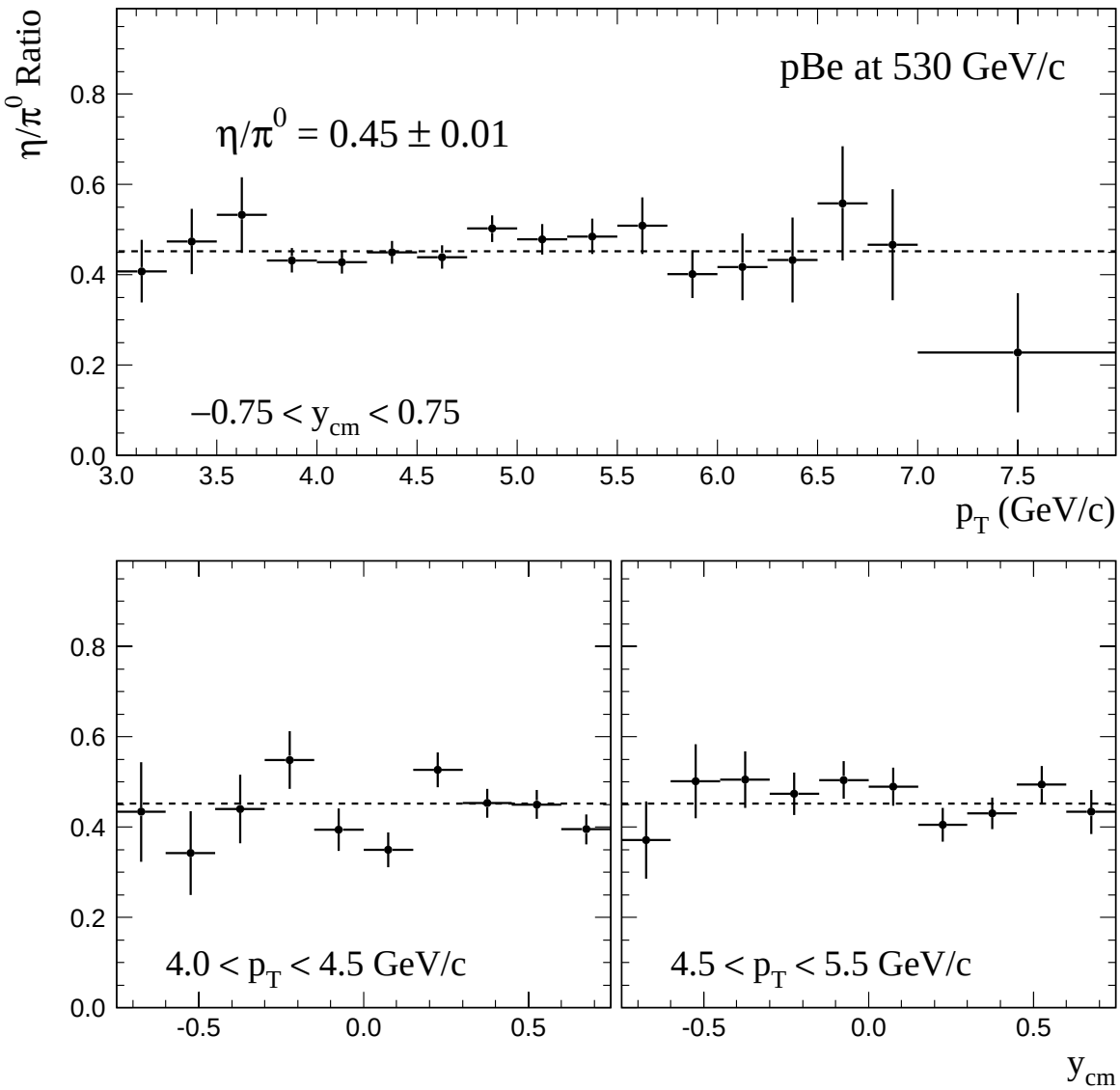

FIG. 24. Ratios of η to π^0 invariant cross sections from 530 GeV/c pBe interactions, as functions of p_T (top), and of $y_{\rm cm}$ (bottom) for two p_T ranges. The error bars reflect only the statistical uncertainties.

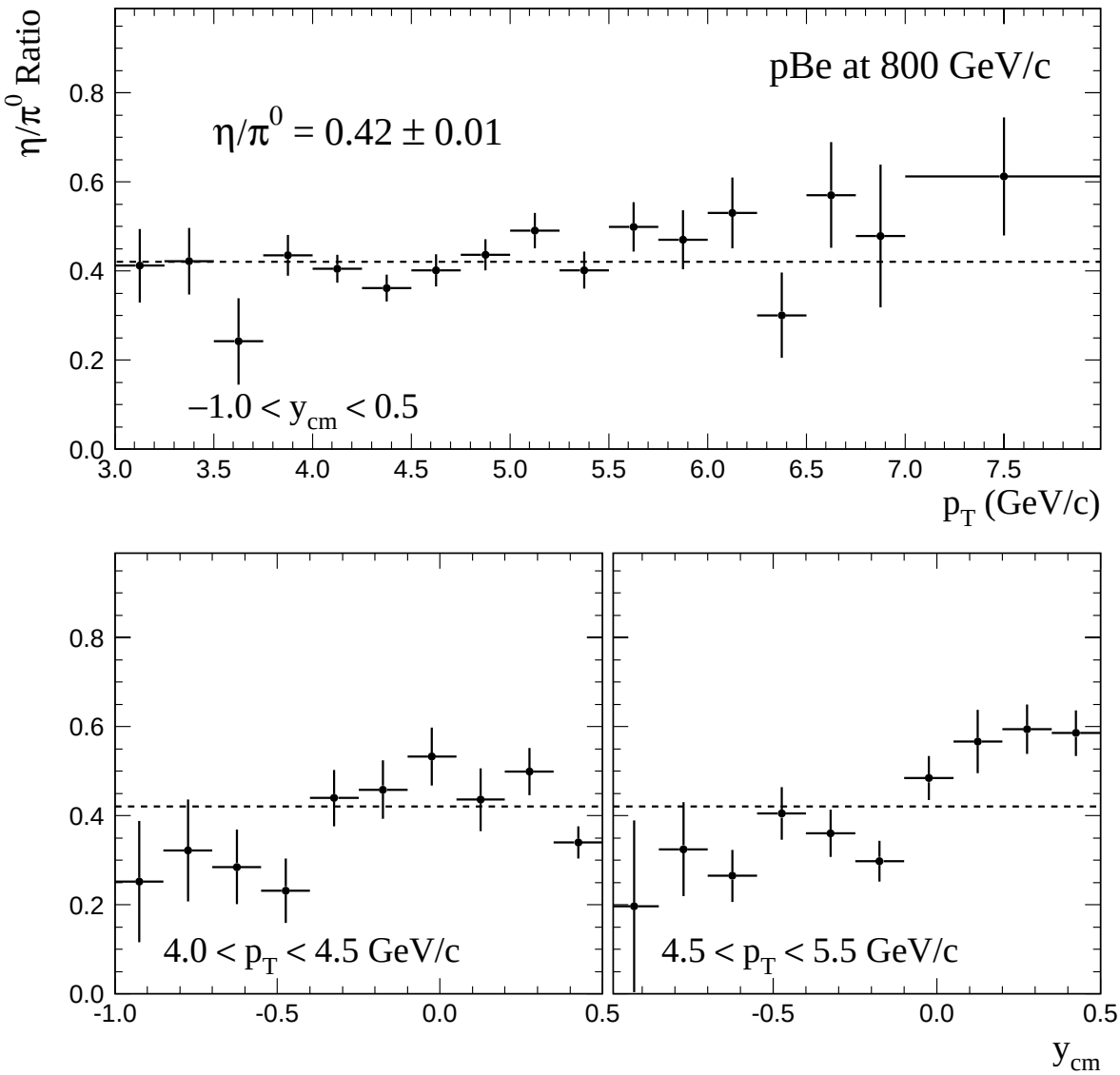

FIG. 25. Ratios of η to π^0 invariant cross sections from 800 GeV/c pBe interactions, as functions of p_T (top), and of $y_{\rm cm}$ (bottom) for two p_T ranges. The error bars reflect only the statistical uncertainties.

TABLES

TABLE I. Compilation of systematic uncertainties for inclusive π^0 and η cross sections. The ranges correspond to variations between low-p_T to high-p_T values.

Source of Uncertainty	π^0 production	η production
Luminosity	8%	8%
Energy Scale	$5\% \rightarrow 9\%$	$5\% \rightarrow 9\%$
Beam Contamination (530 GeV/c beam)	$0\% \rightarrow 7\%$	$0\% \rightarrow 7\%$
Reconstruction Efficiency	5%	6%
Trigger	$2\% \rightarrow 0\%$	$5\% \rightarrow 0\%$
Beam Halo Muon Rejection	1.5%	1%
Geometrical Acceptance	1%	1%
Photon Conversions	1%	1%
Vertex Finding	1%	1%
Background Subtraction	$2\% \rightarrow 0\%$	2%
Total	$11\% \rightarrow 15\%$	$13\% \rightarrow 15\%$

TABLE II. Invariant differential cross sections $\left(Ed^3\sigma/dp^3\right)$ per nucleon for the inclusive reaction pBe $\rightarrow \pi^0$X at 530 and 800 GeV/c, averaged over the rapidity intervals $-0.75 \leq y_{\rm cm} \leq 0.75$ and $-1.0 \leq y_{\rm cm} \leq 0.5$, respectively.

p_T (GeV/c)	pBe @ 530 GeV/c $(\mu b/(GeV/c)^2)$	pBe @ 800 GeV/c $(\mu b/(GeV/c)^2)$
1.00 – 1.20	$467 \pm 29 \pm 49$	$548 \pm 49 \pm 61$
1.20 – 1.40	$199 \pm 14 \pm 21$	$267 \pm 23 \pm 30$
1.40 – 1.60	$68.4 \pm 7.3 \pm 7.2$	$107 \pm 11 \pm 12$
1.60 – 1.80	$26.7 \pm 3.8 \pm 2.8$	$49.3 \pm 5.7 \pm 5.5$
1.80 – 2.00	$15.1 \pm 2.1 \pm 1.6$	$21.5 \pm 3.2 \pm 2.4$
2.00 – 2.20	$6.7 \pm 1.3 \pm 0.71$	$7.3 \pm 1.7 \pm 0.82$
2.20 – 2.30	$2.90 \pm 0.14 \pm 0.31$	$3.92 \pm 0.24 \pm 0.44$
2.30 – 2.40	$1.95 \pm 0.13 \pm 0.21$	$2.67 \pm 0.22 \pm 0.30$
2.40 – 2.50	$1.34 \pm 0.13 \pm 0.14$	$1.77 \pm 0.13 \pm 0.20$
2.50 – 2.60	$0.946 \pm 0.083 \pm 0.10$	$1.208 \pm 0.094 \pm 0.13$
2.60 – 2.70	$0.639 \pm 0.013 \pm 0.068$	$0.818 \pm 0.046 \pm 0.091$
	$(nb/(GeV/c)^2)$	$(nb/(GeV/c)^2)$
2.70 – 2.80	$416.7 \pm 8.3 \pm 44$	$649 \pm 33 \pm 72$
2.80 – 2.90	$286.8 \pm 5.5 \pm 31$	$448 \pm 10 \pm 50$
2.90 – 3.00	$195.5 \pm 4.2 \pm 21$	$317.0 \pm 7.3 \pm 35$
3.00 – 3.10	$135.6 \pm 3.1 \pm 14$	$221.8 \pm 5.3 \pm 25$
3.10 – 3.20	$97.4 \pm 2.7 \pm 10$	$161.7 \pm 4.5 \pm 18$
3.20 – 3.30	$72.9 \pm 2.3 \pm 7.8$	$116.2 \pm 3.3 \pm 13$
3.30 – 3.40	$47.9 \pm 1.4 \pm 5.1$	$91.6 \pm 3.2 \pm 10$
3.40 – 3.50	$35.8 \pm 1.5 \pm 3.8$	$62.1 \pm 2.2 \pm 6.8$
3.50 – 3.60	$25.89 \pm 0.98 \pm 2.7$	$43.9 \pm 1.8 \pm 4.8$
3.60 – 3.70	$17.98 \pm 0.81 \pm 1.9$	$33.6 \pm 1.6 \pm 3.7$
3.70 – 3.80	$13.31 \pm 0.50 \pm 1.4$	$26.4 \pm 1.2 \pm 2.9$
3.80 – 3.90	$10.17 \pm 0.29 \pm 1.1$	$20.6 \pm 1.0 \pm 2.3$
3.90 – 4.00	$7.349 \pm 0.055 \pm 0.78$	$14.56 \pm 0.76 \pm 1.6$
4.00 – 4.10	$5.405 \pm 0.041 \pm 0.58$	$10.86 \pm 0.44 \pm 1.2$
4.10 – 4.20	$4.045 \pm 0.032 \pm 0.43$	$8.59 \pm 0.12 \pm 0.95$
4.20 – 4.30	$3.060 \pm 0.026 \pm 0.33$	$6.443 \pm 0.096 \pm 0.71$
4.30 – 4.40	$2.234 \pm 0.021 \pm 0.24$	$4.706 \pm 0.073 \pm 0.52$
4.40 – 4.50	$1.684 \pm 0.017 \pm 0.18$	$3.657 \pm 0.067 \pm 0.41$
4.50 – 4.60	$1.279 \pm 0.014 \pm 0.14$	$2.831 \pm 0.054 \pm 0.32$
4.60 – 4.70	$0.969 \pm 0.012 \pm 0.10$	$2.159 \pm 0.046 \pm 0.24$
	$(pb/(GeV/c)^2)$	$(pb/(GeV/c)^2)$
4.70 – 4.80	$734 \pm 10 \pm 79$	$1727 \pm 37 \pm 190$
4.80 – 4.90	$556.5 \pm 8.3 \pm 60$	$1343 \pm 24 \pm 150$
4.90 – 5.00	$427.8 \pm 7.1 \pm 47$	$1049 \pm 22 \pm 120$
5.00 – 5.10	$335.0 \pm 6.3 \pm 37$	$811 \pm 18 \pm 91$
5.10 – 5.20	$254.0 \pm 5.2 \pm 28$	$658 \pm 17 \pm 74$
5.20 – 5.30	$197.3 \pm 4.8 \pm 22$	$486 \pm 16 \pm 55$
5.30 – 5.40	$150.5 \pm 3.9 \pm 17$	$411 \pm 13 \pm 46$
5.40 – 5.50	$117.0 \pm 3.4 \pm 13$	$312 \pm 10 \pm 35$
5.50 – 5.60	$88.6 \pm 2.9 \pm 9.8$	$243.7 \pm 7.8 \pm 28$
5.60 – 5.70	$62.4 \pm 2.5 \pm 6.9$	$207.1 \pm 6.8 \pm 24$
5.70 – 5.80	$55.8 \pm 2.3 \pm 6.2$	$159.5 \pm 6.1 \pm 18$
5.80 – 5.90	$43.5 \pm 2.0 \pm 4.9$	$128.6 \pm 5.6 \pm 15$
5.90 – 6.00	$35.1 \pm 1.8 \pm 3.9$	$103.4 \pm 5.3 \pm 12$
6.00 – 6.25	$22.42 \pm 0.85 \pm 2.5$	$74.3 \pm 2.0 \pm 8.5$
6.25 – 6.50	$11.98 \pm 0.61 \pm 1.4$	$43.9 \pm 1.6 \pm 5.1$
6.50 – 6.75	$5.84 \pm 0.41 \pm 0.67$	$23.5 \pm 1.1 \pm 2.7$
6.75 – 7.00	$4.32 \pm 0.35 \pm 0.50$	$15.58 \pm 0.83 \pm 1.8$
7.00 – 7.50	$1.65 \pm 0.15 \pm 0.20$	$7.31 \pm 0.40 \pm 0.87$
7.50 – 8.00	$0.336 \pm 0.066 \pm 0.041$	$2.56 \pm 0.25 \pm 0.31$
8.00 – 9.00	$0.099 \pm 0.024 \pm 0.013$	$0.72 \pm 0.11 \pm 0.09$
9.00 – 10.00	$0.0077 \pm 0.0055 \pm 0.0010$	$0.068 \pm 0.024 \pm 0.009$
10.00 – 12.00	—	$0.020 \pm 0.019 \pm 0.003$

TABLE III. Invariant differential cross sections $\left(Ed^3\sigma/dp^3\right)$ for the inclusive reaction $pp \to \pi^0$X at 530 and 800 GeV/c, averaged over the rapidity intervals $-0.75 \leq y_{\rm cm} \leq 0.75$ and $-1.0 \leq y_{\rm cm} \leq 0.5$, respectively.

p_T (GeV/c)	pp @ 530 GeV/c $(\mu b/(GeV/c)^2)$	pp @ 800 GeV/c $(\mu b/(GeV/c)^2)$
1.00 – 1.40	$284 \pm 44 \pm 30$	$531 \pm 72 \pm 59$
1.40 – 1.80	$63 \pm 10 \pm 6.7$	$113 \pm 17 \pm 13$
1.80 – 2.20	$13.5 \pm 3.6 \pm 1.4$	$17.3 \pm 5.2 \pm 1.9$
2.20 – 2.40	$3.36 \pm 0.81 \pm 0.36$	$3.25 \pm 0.43 \pm 0.36$
2.40 – 2.60	$1.15 \pm 0.14 \pm 0.12$	$1.33 \pm 0.22 \pm 0.15$
	$(nb/(GeV/c)^2)$	$(nb/(GeV/c)^2)$
2.60 – 2.80	$475 \pm 17 \pm 51$	$693 \pm 57 \pm 77$
2.80 – 3.00	$205.2 \pm 7.4 \pm 22$	$315 \pm 13 \pm 35$
3.00 – 3.20	$98.9 \pm 4.6 \pm 11$	$171.7 \pm 7.7 \pm 19$
3.20 – 3.40	$52.5 \pm 3.3 \pm 5.6$	$91.7 \pm 4.7 \pm 10$
3.40 – 3.60	$25.6 \pm 1.7 \pm 2.7$	$47.4 \pm 3.5 \pm 5.2$
3.60 – 3.80	$12.63 \pm 0.99 \pm 1.3$	$25.7 \pm 2.3 \pm 2.8$
3.80 – 4.00	$7.22 \pm 0.24 \pm 0.77$	$14.7 \pm 1.3 \pm 1.6$
4.00 – 4.20	$4.170 \pm 0.060 \pm 0.45$	$9.18 \pm 0.65 \pm 1.0$
4.20 – 4.40	$2.263 \pm 0.037 \pm 0.24$	$5.03 \pm 0.15 \pm 0.56$
4.40 – 4.60	$1.279 \pm 0.027 \pm 0.14$	$2.906 \pm 0.099 \pm 0.32$
	$(pb/(GeV/c)^2)$	$(pb/(GeV/c)^2)$
4.60 – 4.80	$757 \pm 18 \pm 82$	$1688 \pm 64 \pm 190$
4.80 – 5.00	$450 \pm 13 \pm 49$	$1057 \pm 36 \pm 120$
5.00 – 5.20	$279.6 \pm 9.5 \pm 31$	$600 \pm 27 \pm 67$
5.20 – 5.40	$164.3 \pm 7.6 \pm 18$	$400 \pm 21 \pm 45$
5.40 – 5.60	$101.4 \pm 5.4 \pm 11$	$256 \pm 17 \pm 29$
5.60 – 5.80	$59.9 \pm 4.0 \pm 6.7$	$163 \pm 11 \pm 19$
5.80 – 6.00	$38.3 \pm 3.3 \pm 4.3$	$98.4 \pm 7.9 \pm 11$
6.00 – 6.25	$22.5 \pm 2.1 \pm 2.5$	$75.8 \pm 5.3 \pm 8.7$
6.25 – 6.50	$11.1 \pm 1.5 \pm 1.3$	$34.2 \pm 3.1 \pm 4.0$
6.50 – 6.75	$5.53 \pm 0.94 \pm 0.64$	$27.6 \pm 2.6 \pm 3.2$
6.75 – 7.00	$4.15 \pm 0.80 \pm 0.48$	$12.3 \pm 1.9 \pm 1.5$
7.00 – 7.50	$1.35 \pm 0.31 \pm 0.16$	$8.2 \pm 1.2 \pm 0.98$
7.50 – 8.00	$0.70 \pm 0.23 \pm 0.09$	$3.35 \pm 0.65 \pm 0.41$
8.00 – 9.00	$0.185 \pm 0.093 \pm 0.023$	$0.67 \pm 0.19 \pm 0.08$
9.00 – 10.00	—	$0.083 \pm 0.098 \pm 0.011$
10.00 – 12.00	—	$0.016 \pm 0.016 \pm 0.002$

TABLE IV. The averaged invariant differential cross section per nucleon $\left(Ed^3\sigma/dp^3\right)$ as a function of rapidity and p_T for the inclusive reaction pBe $\rightarrow \pi^0$X at 530 GeV/c.

y_{cm}	p_T (GeV/c)			
	1.00 – 1.50 ($\mu b/(GeV/c)^2$)	1.50 – 2.00 ($\mu b/(GeV/c)^2$)	2.00 – 2.50 ($\mu b/(GeV/c)^2$)	2.50 – 3.00 ($nb/(GeV/c)^2$)
−0.750 – −0.625	388 ± 43 ± 41	27.2 ± 7.9 ± 2.9	6.5 ± 1.6 ± 0.7	820 ± 180 ± 90
−0.625 – −0.500				409 ± 86 ± 44
−0.500 – −0.375	313 ± 40 ± 33	25.5 ± 6.0 ± 2.7	2.9 ± 1.2 ± 0.3	496 ± 23 ± 53
−0.375 – −0.250				494 ± 15 ± 53
−0.250 – −0.125	324 ± 33 ± 34	29.7 ± 6.2 ± 3.1	4.1 ± 1.2 ± 0.4	513 ± 12 ± 55
−0.125 – 0.000				587 ± 13 ± 63
0.000 – 0.125	233 ± 30 ± 25	33.4 ± 5.7 ± 3.5	5.1 ± 1.2 ± 0.5	527.8 ± 9.8 ± 56
0.125 – 0.250				502.0 ± 8.2 ± 54
0.250 – 0.375	241 ± 29 ± 25	31.5 ± 4.9 ± 3.3	2.7 ± 1.3 ± 0.3	455.3 ± 7.6 ± 49
0.375 – 0.500				427.6 ± 7.5 ± 46
0.500 – 0.625	293 ± 29 ± 31	17.5 ± 5.0 ± 1.9	2.28 ± 0.97 ± 0.24	387.0 ± 8.0 ± 41
0.625 – 0.750				341.8 ± 7.8 ± 36
	3.00 – 3.50 ($nb/(GeV/c)^2$)	3.50 – 4.00 ($nb/(GeV/c)^2$)	4.00 – 4.50 ($nb/(GeV/c)^2$)	4.50 – 5.00 ($nb/(GeV/c)^2$)
−0.750 – −0.625	68.5 ± 4.6 ± 7.3	9.55 ± 0.66 ± 1.0	2.527 ± 0.065 ± 0.27	0.585 ± 0.020 ± 0.063
−0.625 – −0.500	85.3 ± 5.5 ± 9.1	13.9 ± 1.2 ± 1.5	2.866 ± 0.062 ± 0.31	0.677 ± 0.019 ± 0.073
−0.500 – −0.375	78.8 ± 5.1 ± 8.4	14.2 ± 1.0 ± 1.5	3.264 ± 0.053 ± 0.35	0.783 ± 0.018 ± 0.085
−0.375 – −0.250	81.0 ± 3.2 ± 8.7	17.1 ± 1.1 ± 1.8	3.599 ± 0.051 ± 0.39	0.905 ± 0.018 ± 0.098
−0.250 – −0.125	89.5 ± 3.3 ± 9.6	17.8 ± 1.1 ± 1.9	3.864 ± 0.042 ± 0.41	0.963 ± 0.017 ± 0.10
−0.125 – 0.000	91.4 ± 3.3 ± 9.8	20.0 ± 1.2 ± 2.1	4.185 ± 0.041 ± 0.45	1.038 ± 0.017 ± 0.11
0.000 – 0.125	88.5 ± 2.9 ± 9.4	17.30 ± 0.96 ± 1.8	4.001 ± 0.038 ± 0.43	0.927 ± 0.015 ± 0.10
0.125 – 0.250	77.7 ± 2.4 ± 8.3	15.47 ± 0.73 ± 1.6	3.720 ± 0.035 ± 0.40	0.931 ± 0.015 ± 0.10
0.250 – 0.375	78.9 ± 2.5 ± 8.4	16.77 ± 0.85 ± 1.8	3.420 ± 0.032 ± 0.37	0.872 ± 0.015 ± 0.094
0.375 – 0.500	74.6 ± 2.6 ± 8.0	13.15 ± 0.77 ± 1.4	3.150 ± 0.034 ± 0.34	0.743 ± 0.014 ± 0.080
0.500 – 0.625	65.4 ± 2.6 ± 7.0	13.9 ± 1.0 ± 1.5	2.670 ± 0.033 ± 0.29	0.629 ± 0.014 ± 0.068
0.625 – 0.750	55.5 ± 2.6 ± 5.9	10.14 ± 0.89 ± 1.1	2.159 ± 0.030 ± 0.23	0.469 ± 0.013 ± 0.051
	5.00 – 5.50 ($pb/(GeV/c)^2$)	5.50 – 6.50 ($pb/(GeV/c)^2$)	6.50 – 8.00 ($pb/(GeV/c)^2$)	8.00 – 10.00 ($pb/(GeV/c)^2$)
−0.750 – −0.625	144.3 ± 7.6 ± 16	24.9 ± 2.0 ± 2.8	1.51 ± 0.22 ± 0.18	0.015 ± 0.027 ± 0.002
−0.625 – −0.500	202.1 ± 8.6 ± 22	28.9 ± 1.9 ± 3.2		
−0.500 – −0.375	215.9 ± 7.7 ± 24	40.0 ± 2.1 ± 4.5	2.02 ± 0.23 ± 0.24	0.053 ± 0.027 ± 0.007
−0.375 – −0.250	236.4 ± 7.8 ± 26	44.0 ± 2.2 ± 4.9		
−0.250 – −0.125	253.7 ± 7.9 ± 28	48.4 ± 2.3 ± 5.4	3.31 ± 0.30 ± 0.39	0.059 ± 0.030 ± 0.007
−0.125 – 0.000	268.0 ± 8.2 ± 29	50.2 ± 2.3 ± 5.6		
0.000 – 0.125	251.5 ± 7.4 ± 28	46.1 ± 2.1 ± 5.2	3.04 ± 0.27 ± 0.36	0.152 ± 0.050 ± 0.019
0.125 – 0.250	268.7 ± 7.7 ± 29	45.5 ± 2.1 ± 5.1		
0.250 – 0.375	230.7 ± 7.2 ± 25	42.7 ± 2.0 ± 4.8	2.68 ± 0.28 ± 0.32	0.029 ± 0.021 ± 0.004
0.375 – 0.500	182.8 ± 6.6 ± 20	34.7 ± 1.9 ± 3.9		
0.500 – 0.625	164.0 ± 6.6 ± 18	24.8 ± 1.8 ± 2.8	1.58 ± 0.23 ± 0.19	0.014 ± 0.014 ± 0.002
0.625 – 0.750	111.0 ± 5.7 ± 12	15.6 ± 1.4 ± 1.7		

TABLE V. The averaged invariant differential cross section $\left(Ed^3\sigma/dp^3\right)$ as a function of rapidity and p_T for the inclusive reaction $pp \to \pi^0$X at 530 GeV/c.

y_{cm}	p_T (GeV/c)			
	1.00 – 2.50 ($\mu b/(GeV/c)^2$)	2.50 – 3.00 ($nb/(GeV/c)^2$)	3.00 – 3.50 ($nb/(GeV/c)^2$)	3.50 – 4.00 ($nb/(GeV/c)^2$)
−0.750 – −0.625	147 ± 15 ± 16	540 ± 180 ± 60	68 ± 10 ± 7	8.7 ± 1.4 ± 0.9
−0.625 – −0.500		950 ± 330 ± 100	66 ± 15 ± 7	10.0 ± 1.4 ± 1.1
−0.500 – −0.375	119 ± 15 ± 13	365 ± 40 ± 39	61 ± 10 ± 6	12.3 ± 2.7 ± 1.3
−0.375 – −0.250		440 ± 39 ± 47	65.5 ± 7.2 ± 7.0	14.9 ± 2.3 ± 1.6
−0.250 – −0.125	123 ± 12 ± 13	458 ± 26 ± 49	76.7 ± 6.9 ± 8.2	15.4 ± 2.4 ± 1.6
−0.125 – 0.000		534 ± 32 ± 57	81.7 ± 7.2 ± 8.7	14.6 ± 2.5 ± 1.5
0.000 – 0.125	91 ± 11 ± 10	457 ± 20 ± 49	78.7 ± 6.5 ± 8.4	13.5 ± 2.2 ± 1.4
0.125 – 0.250		424 ± 19 ± 45	67.8 ± 5.4 ± 7.2	13.5 ± 1.7 ± 1.4
0.250 – 0.375	96 ± 11 ± 10	398 ± 18 ± 42	63.5 ± 5.7 ± 6.8	11.2 ± 1.6 ± 1.2
0.375 – 0.500		369 ± 17 ± 39	62.7 ± 5.9 ± 6.7	14.1 ± 2.0 ± 1.5
0.500 – 0.625	116 ± 11 ± 12	347 ± 18 ± 37	57.2 ± 6.1 ± 6.1	11.1 ± 2.2 ± 1.2
0.625 – 0.750		303 ± 18 ± 32	49.4 ± 5.9 ± 5.3	7.8 ± 1.6 ± 0.8
	4.00 – 4.50 ($nb/(GeV/c)^2$)	4.50 – 5.00 ($nb/(GeV/c)^2$)	5.00 – 5.50 ($pb/(GeV/c)^2$)	5.50 – 6.50 ($pb/(GeV/c)^2$)
−0.750 – −0.625	2.02 ± 0.15 ± 0.22	0.610 ± 0.062 ± 0.066	104 ± 13 ± 11	27.5 ± 4.6 ± 3.1
−0.625 – −0.500	2.46 ± 0.14 ± 0.26	0.515 ± 0.046 ± 0.056	166 ± 21 ± 18	21.0 ± 4.2 ± 2.4
−0.500 – −0.375	2.74 ± 0.11 ± 0.29	0.645 ± 0.036 ± 0.070	207 ± 18 ± 23	40.5 ± 5.4 ± 4.6
−0.375 – −0.250	3.34 ± 0.12 ± 0.36	0.833 ± 0.045 ± 0.090	192 ± 17 ± 21	39.6 ± 4.9 ± 4.4
−0.250 – −0.125	3.318 ± 0.091 ± 0.36	0.809 ± 0.037 ± 0.087	231 ± 18 ± 25	41.0 ± 5.2 ± 4.6
−0.125 – 0.000	3.555 ± 0.095 ± 0.38	0.917 ± 0.040 ± 0.099	239 ± 19 ± 26	62.9 ± 6.4 ± 7.1
0.000 – 0.125	3.565 ± 0.092 ± 0.38	0.807 ± 0.034 ± 0.087	266 ± 19 ± 29	52.1 ± 5.5 ± 5.8
0.125 – 0.250	3.316 ± 0.083 ± 0.36	0.848 ± 0.037 ± 0.092	249 ± 18 ± 27	52.5 ± 5.6 ± 5.9
0.250 – 0.375	2.960 ± 0.072 ± 0.32	0.723 ± 0.033 ± 0.078	235 ± 18 ± 26	38.7 ± 4.8 ± 4.3
0.375 – 0.500	2.791 ± 0.078 ± 0.30	0.683 ± 0.033 ± 0.074	200 ± 17 ± 22	29.7 ± 4.2 ± 3.3
0.500 – 0.625	2.356 ± 0.075 ± 0.25	0.624 ± 0.034 ± 0.067	179 ± 17 ± 20	25.3 ± 4.2 ± 2.8
0.625 – 0.750	1.917 ± 0.069 ± 0.21	0.451 ± 0.030 ± 0.049	116 ± 14 ± 13	21.8 ± 4.1 ± 2.4
	6.50 – 8.00 ($pb/(GeV/c)^2$)			
−0.750 – −0.625	2.00 ± 0.57 ± 0.24			
−0.625 – −0.500				
−0.500 – −0.375	2.62 ± 0.66 ± 0.31			
−0.375 – −0.250				
−0.250 – −0.125	3.00 ± 0.70 ± 0.35			
−0.125 – 0.000				
0.000 – 0.125	3.62 ± 0.70 ± 0.43			
0.125 – 0.250				
0.250 – 0.375	1.70 ± 0.50 ± 0.20			
0.375 – 0.500				
0.500 – 0.625	0.91 ± 0.41 ± 0.11			
0.625 – 0.750				

TABLE VI. The averaged invariant differential cross sections per nucleon $\left(Ed^3\sigma/dp^3\right)$ as a function of rapidity and p_T for the inclusive reaction pBe $\rightarrow \pi^0$X at 800 GeV/c.

y_{cm}	p_T (GeV/c)			
	1.00 – 1.50 ($\mu b/(GeV/c)^2$)	1.50 – 2.00 ($\mu b/(GeV/c)^2$)	2.00 – 2.50 ($\mu b/(GeV/c)^2$)	2.50 – 3.00 ($nb/(GeV/c)^2$)
−1.00 – −0.875	444 ± 71 ± 49	36 ± 11 ± 4	6.5 ± 1.9 ± 0.7	477 ± 87 ± 53
−0.875 – −0.750				840 ± 180 ± 90
−0.750 – −0.625	297 ± 65 ± 33	58.8 ± 9.0 ± 6.5	5.9 ± 1.8 ± 0.7	615 ± 55 ± 68
−0.625 – −0.500				686 ± 50 ± 76
−0.500 – −0.375	372 ± 59 ± 41	57.1 ± 9.4 ± 6.3	1.3 ± 1.8 ± 0.1	610 ± 50 ± 68
−0.375 – −0.250				705 ± 51 ± 78
−0.250 – −0.125	304 ± 53 ± 34	55.1 ± 8.5 ± 6.1	4.1 ± 1.6 ± 0.5	758 ± 45 ± 84
−0.125 – 0.000				732 ± 46 ± 81
0.000 – 0.125	269 ± 46 ± 30	45.3 ± 7.7 ± 5.0	5.4 ± 1.6 ± 0.6	766 ± 47 ± 85
0.125 – 0.250				730 ± 100 ± 80
0.250 – 0.375	409 ± 45 ± 45	31.6 ± 7.6 ± 3.5	4.5 ± 1.4 ± 0.5	750 ± 49 ± 83
0.375 – 0.500				588 ± 42 ± 65
	3.00 – 3.50 ($nb/(GeV/c)^2$)	3.50 – 4.00 ($nb/(GeV/c)^2$)	4.00 – 4.50 ($nb/(GeV/c)^2$)	4.50 – 5.00 ($nb/(GeV/c)^2$)
−1.00 – −0.875	100.5 ± 8.1 ± 11	20.0 ± 2.0 ± 2.2	4.01 ± 0.28 ± 0.44	1.039 ± 0.036 ± 0.12
−0.875 – −0.750	124.1 ± 7.6 ± 14	22.4 ± 2.2 ± 2.5	4.73 ± 0.37 ± 0.52	1.180 ± 0.036 ± 0.13
−0.750 – −0.625	102.3 ± 6.1 ± 11	25.8 ± 2.5 ± 2.8	5.58 ± 0.31 ± 0.62	1.512 ± 0.038 ± 0.17
−0.625 – −0.500	118.4 ± 5.2 ± 13	25.2 ± 1.9 ± 2.8	7.62 ± 0.45 ± 0.84	1.785 ± 0.042 ± 0.20
−0.500 – −0.375	143.0 ± 6.4 ± 16	30.0 ± 2.1 ± 3.3	7.40 ± 0.40 ± 0.82	2.029 ± 0.037 ± 0.23
−0.375 – −0.250	144.5 ± 5.7 ± 16	32.3 ± 2.1 ± 3.6	8.00 ± 0.36 ± 0.89	2.101 ± 0.035 ± 0.23
−0.250 – −0.125	149.0 ± 5.7 ± 17	28.1 ± 2.2 ± 3.1	7.91 ± 0.32 ± 0.88	2.168 ± 0.036 ± 0.24
−0.125 – 0.000	144.4 ± 5.8 ± 16	29.9 ± 2.3 ± 3.3	7.75 ± 0.37 ± 0.86	2.192 ± 0.038 ± 0.24
0.000 – 0.125	142.1 ± 4.8 ± 16	32.1 ± 1.8 ± 3.5	7.96 ± 0.29 ± 0.88	2.129 ± 0.087 ± 0.24
0.125 – 0.250	143.4 ± 4.6 ± 16	29.5 ± 1.7 ± 3.3	7.62 ± 0.28 ± 0.84	2.02 ± 0.10 ± 0.23
0.250 – 0.375	129.3 ± 4.9 ± 14	29.5 ± 1.8 ± 3.2	6.88 ± 0.22 ± 0.76	1.877 ± 0.086 ± 0.21
0.375 – 0.500	127.3 ± 5.5 ± 14	29.2 ± 2.1 ± 3.2	6.76 ± 0.24 ± 0.75	1.828 ± 0.084 ± 0.20
	5.00 – 5.50 ($pb/(GeV/c)^2$)	5.50 – 6.50 ($pb/(GeV/c)^2$)	6.50 – 8.00 ($pb/(GeV/c)^2$)	8.00 – 10.00 ($pb/(GeV/c)^2$)
−1.00 – −0.875	268 ± 25 ± 30	54.3 ± 3.7 ± 6.2	3.54 ± 0.42 ± 0.42	—
−0.875 – −0.750	326 ± 16 ± 37	68.1 ± 4.3 ± 7.8		
−0.750 – −0.625	411 ± 16 ± 46	82.8 ± 4.1 ± 9.5	7.51 ± 0.63 ± 0.89	0.10 ± 0.10 ± 0.01
−0.625 – −0.500	505 ± 19 ± 57	109.3 ± 5.6 ± 13		
−0.500 – −0.375	595 ± 18 ± 67	120.5 ± 4.9 ± 14	11.18 ± 0.70 ± 1.3	0.50 ± 0.11 ± 0.06
−0.375 – −0.250	635 ± 17 ± 72	141.5 ± 5.3 ± 16		
−0.250 – −0.125	646 ± 18 ± 73	142.2 ± 5.0 ± 16	12.70 ± 0.75 ± 1.5	0.60 ± 0.16 ± 0.07
−0.125 – 0.000	639 ± 19 ± 72	135.2 ± 5.2 ± 15		
0.000 – 0.125	645 ± 28 ± 73	137.7 ± 6.1 ± 16	13.96 ± 0.78 ± 1.7	0.76 ± 0.15 ± 0.09
0.125 – 0.250	646 ± 37 ± 73	132.4 ± 7.2 ± 15		
0.250 – 0.375	583 ± 29 ± 66	134.1 ± 6.5 ± 15	9.93 ± 0.73 ± 1.2	0.48 ± 0.16 ± 0.06
0.375 – 0.500	526 ± 27 ± 59	107.0 ± 6.0 ± 12		

TABLE VII. The averaged invariant differential cross sections $\left(Ed^3\sigma/dp^3\right)$ as a function of rapidity and p_T for the inclusive reaction $pp \to \pi^0$X at 800 GeV/c.

y_{cm}	p_T (GeV/c)			
	1.00 – 2.50 ($\mu b/(GeV/c)^2$)	2.50 – 3.00 ($nb/(GeV/c)^2$)	3.00 – 3.50 ($nb/(GeV/c)^2$)	3.50 – 4.00 ($nb/(GeV/c)^2$)
−1.00 – −0.875	166 ± 26 ± 18	980 ± 580 ± 110	83 ± 16 ± 9	19.2 ± 7.4 ± 2.1
−0.875 – −0.750		410 ± 110 ± 50	108 ± 14 ± 12	18.7 ± 4.1 ± 2.1
−0.750 – −0.625	120 ± 24 ± 13	420 ± 63 ± 47	101 ± 14 ± 11	36.9 ± 6.9 ± 4.1
−0.625 – −0.500		570 ± 100 ± 60	111 ± 12 ± 12	18.0 ± 3.6 ± 2.0
−0.500 – −0.375	146 ± 21 ± 16	560 ± 110 ± 60	144 ± 14 ± 16	26.6 ± 5.5 ± 2.9
−0.375 – −0.250		600 ± 99 ± 67	130 ± 13 ± 14	37.1 ± 6.0 ± 4.1
−0.250 – −0.125	130 ± 20 ± 14	760 ± 170 ± 90	117 ± 14 ± 13	31.0 ± 5.2 ± 3.4
−0.125 – 0.000		640 ± 110 ± 70	117 ± 12 ± 13	20.6 ± 4.1 ± 2.3
0.000 – 0.125	115 ± 17 ± 13	669 ± 95 ± 74	127 ± 11 ± 14	23.7 ± 4.5 ± 2.6
0.125 – 0.250		720 ± 110 ± 80	130 ± 10 ± 14	26.3 ± 4.0 ± 2.9
0.250 – 0.375	164 ± 16 ± 18	511 ± 84 ± 57	115 ± 11 ± 13	22.5 ± 3.6 ± 2.5
0.375 – 0.500		699 ± 97 ± 78	102 ± 12 ± 11	22.4 ± 5.1 ± 2.5
	4.00 – 4.50 ($nb/(GeV/c)^2$)	4.50 – 5.00 ($nb/(GeV/c)^2$)	5.00 – 5.50 ($pb/(GeV/c)^2$)	5.50 – 6.50 ($pb/(GeV/c)^2$)
−1.00 – −0.875	3.02 ± 0.25 ± 0.34	1.18 ± 0.12 ± 0.13	280 ± 46 ± 32	30.3 ± 5.2 ± 3.5
−0.875 – −0.750	4.66 ± 0.65 ± 0.52	0.957 ± 0.072 ± 0.11	217 ± 25 ± 24	70 ± 13 ± 8
−0.750 – −0.625	8.4 ± 2.2 ± 0.9	1.350 ± 0.085 ± 0.15	331 ± 34 ± 37	60.2 ± 8.2 ± 6.9
−0.625 – −0.500	7.4 ± 1.5 ± 0.8	1.504 ± 0.093 ± 0.17	423 ± 36 ± 48	99 ± 12 ± 11
−0.500 – −0.375	6.41 ± 0.63 ± 0.71	1.808 ± 0.087 ± 0.20	479 ± 41 ± 54	84.9 ± 9.7 ± 9.7
−0.375 – −0.250	6.86 ± 0.61 ± 0.76	1.901 ± 0.081 ± 0.21	517 ± 39 ± 58	124 ± 12 ± 14
−0.250 – −0.125	6.00 ± 0.20 ± 0.66	1.963 ± 0.083 ± 0.22	595 ± 41 ± 67	110 ± 11 ± 13
−0.125 – 0.000	6.14 ± 0.35 ± 0.68	1.878 ± 0.081 ± 0.21	552 ± 38 ± 62	140 ± 13 ± 16
0.000 – 0.125	8.2 ± 1.0 ± 0.9	1.49 ± 0.13 ± 0.17	607 ± 68 ± 68	150 ± 17 ± 17
0.125 – 0.250	6.19 ± 0.57 ± 0.69	1.71 ± 0.22 ± 0.19	567 ± 88 ± 64	111 ± 14 ± 13
0.250 – 0.375	7.08 ± 0.57 ± 0.78	1.68 ± 0.20 ± 0.19	459 ± 61 ± 52	97 ± 12 ± 11
0.375 – 0.500	5.69 ± 0.52 ± 0.63	1.81 ± 0.21 ± 0.20	502 ± 64 ± 57	129 ± 16 ± 15
	6.50 – 8.00 ($pb/(GeV/c)^2$)	8.00 – 10.00 ($pb/(GeV/c)^2$)		
−1.00 – −0.875	4.20 ± 1.00 ± 0.50	0.085 ± 0.085 ± 0.010		
−0.875 – −0.750				
−0.750 – −0.625	8.8 ± 1.6 ± 1.0	0.23 ± 0.17 ± 0.03		
−0.625 – −0.500				
−0.500 – −0.375	14.0 ± 1.8 ± 1.7	0.53 ± 0.24 ± 0.07		
−0.375 – −0.250				
−0.250 – −0.125	13.8 ± 1.7 ± 1.6	0.95 ± 0.43 ± 0.12		
−0.125 – 0.000				
0.000 – 0.125	12.7 ± 2.1 ± 1.5	0.66 ± 0.30 ± 0.08		
0.125 – 0.250				
0.250 – 0.375	9.6 ± 1.7 ± 1.1	—		
0.375 – 0.500				

TABLE VIII. Invariant differential cross sections $\left(Ed^3\sigma/dp^3\right)$ per nucleon for the inclusive reaction pBe $\to \eta$X at 530 and 800 GeV/c, averaged over the rapidity intervals $-0.75 \leq y_{\rm cm} \leq 0.75$ and $-1.0 \leq y_{\rm cm} \leq 0.5$, respectively.

p_T (GeV/c)	pBe @ 530 GeV/c $(nb/(GeV/c)^2)$	pBe @ 800 GeV/c $(nb/(GeV/c)^2)$
3.00 – 3.20	$49.2 \pm 9.0 \pm 6.0$	$88 \pm 18 \pm 11$
3.20 – 3.40	$24.4 \pm 4.5 \pm 2.9$	$34.7 \pm 8.5 \pm 4.3$
3.40 – 3.60	$16.3 \pm 2.5 \pm 1.9$	$19.5 \pm 5.1 \pm 2.4$
3.60 – 3.80	$8.5 \pm 1.4 \pm 0.98$	$8.1 \pm 3.0 \pm 0.96$
3.80 – 4.00	$3.67 \pm 0.25 \pm 0.42$	$7.34 \pm 0.77 \pm 0.86$
4.00 – 4.20	$2.00 \pm 0.13 \pm 0.23$	$3.89 \pm 0.33 \pm 0.45$
4.20 – 4.40	$1.242 \pm 0.078 \pm 0.14$	$2.18 \pm 0.19 \pm 0.25$
4.40 – 4.60	$0.587 \pm 0.043 \pm 0.067$	$1.20 \pm 0.12 \pm 0.14$
4.60 – 4.80	$0.409 \pm 0.024 \pm 0.047$	$0.805 \pm 0.073 \pm 0.095$
4.80 – 5.00	$0.244 \pm 0.017 \pm 0.028$	$0.502 \pm 0.048 \pm 0.059$
	$(pb/(GeV/c)^2)$	$(pb/(GeV/c)^2)$
5.00 – 5.25	$132.5 \pm 9.2 \pm 15$	$341 \pm 27 \pm 40$
5.25 – 5.50	$70.2 \pm 5.6 \pm 8.2$	$152 \pm 15 \pm 18$
5.50 – 5.75	$36.3 \pm 4.4 \pm 4.3$	$107 \pm 12 \pm 13$
5.75 – 6.00	$17.2 \pm 2.2 \pm 2.0$	$58.0 \pm 8.0 \pm 7.0$
6.00 – 6.50	$7.27 \pm 0.98 \pm 0.87$	$26.3 \pm 3.6 \pm 3.2$
6.50 – 7.00	$2.63 \pm 0.43 \pm 0.32$	$10.4 \pm 1.8 \pm 1.3$
7.00 – 8.00	$0.23 \pm 0.13 \pm 0.028$	$3.02 \pm 0.64 \pm 0.38$
8.00 – 9.00	$0.035 \pm 0.046 \pm 0.005$	$1.33 \pm 0.43 \pm 0.17$
9.00 – 10.00	—	$0.11 \pm 0.24 \pm 0.015$
10.00 – 12.00	—	$0.073 \pm 0.050 \pm 0.010$

TABLE IX. Invariant differential cross sections $\left(Ed^3\sigma/dp^3\right)$ for the inclusive reaction $pp \to \eta$X at 530 and 800 GeV/c, averaged over the rapidity intervals $-0.75 \leq y_{\rm cm} \leq 0.75$ and $-1.0 \leq y_{\rm cm} \leq 0.5$, respectively.

p_T (GeV/c)	pp @ 530 GeV/c $(nb/(GeV/c)^2)$	pp @ 800 GeV/c $(nb/(GeV/c)^2)$
3.00 – 3.50	$22.6 \pm 9.5 \pm 2.7$	$51 \pm 17 \pm 6.3$
3.50 – 4.00	$7.6 \pm 1.9 \pm 0.87$	$11.4 \pm 3.7 \pm 1.4$
4.00 – 4.50	$1.19 \pm 0.14 \pm 0.13$	$2.13 \pm 0.34 \pm 0.25$
4.50 – 5.00	$0.310 \pm 0.035 \pm 0.035$	$0.678 \pm 0.091 \pm 0.080$
	$(pb/(GeV/c)^2)$	$(pb/(GeV/c)^2)$
5.00 – 5.50	$77 \pm 12 \pm 9.0$	$220 \pm 36 \pm 26$
5.50 – 6.00	$23.7 \pm 5.0 \pm 2.8$	$108 \pm 16 \pm 13$
6.00 – 7.00	$2.3 \pm 1.2 \pm 0.3$	$20.6 \pm 4.8 \pm 2.5$
7.00 – 8.00	$0.41 \pm 0.31 \pm 0.05$	$4.4 \pm 1.8 \pm 0.6$
8.00 – 10.00	—	$1.05 \pm 0.70 \pm 0.14$

TABLE X. The averaged invariant differential cross sections per nucleon $\left(Ed^3\sigma/dp^3\right)$ as a function of rapidity and p_T for the inclusive reaction pBe $\rightarrow \eta$X at 530 GeV/c. The units are pb/(GeV/c)^2.

y_{cm}	p_T (GeV/c) 3.00 – 4.00	4.00 – 4.50	4.50 – 5.00	5.00 – 5.50
−0.750 – −0.625	14600 ± 9000 ± 1600	1050 ± 310 ± 110	247 ± 62 ± 27	66 ± 25 ± 7
−0.625 – −0.500		950 ± 320 ± 100	318 ± 88 ± 34	96 ± 20 ± 10
−0.500 – −0.375	24100 ± 4900 ± 2600	1420 ± 280 ± 150	374 ± 68 ± 40	100 ± 26 ± 11
−0.375 – −0.250		1730 ± 290 ± 190	431 ± 60 ± 47	111 ± 18 ± 12
−0.250 – −0.125	21200 ± 3800 ± 2300	1930 ± 250 ± 210	486 ± 57 ± 52	134 ± 19 ± 15
−0.125 – 0.000		1750 ± 200 ± 190	514 ± 56 ± 56	123 ± 17 ± 13
0.000 – 0.125	26700 ± 3400 ± 2900	1330 ± 170 ± 140	482 ± 51 ± 52	121 ± 18 ± 13
0.125 – 0.250		2060 ± 160 ± 220	364 ± 45 ± 39	97 ± 15 ± 11
0.250 – 0.375	22700 ± 3300 ± 2400	1480 ± 120 ± 160	333 ± 39 ± 36	129 ± 20 ± 14
0.375 – 0.500		1390 ± 100 ± 150	327 ± 34 ± 35	94 ± 15 ± 10
0.500 – 0.625	13200 ± 4100 ± 1400	1220 ± 100 ± 130	321 ± 36 ± 35	90 ± 14 ± 10
0.625 – 0.750		837 ± 74 ± 89	187 ± 28 ± 20	56 ± 12 ± 6

	5.50 – 6.50	6.50 – 8.00
−0.750 – −0.625	4.6 ± 7.0 ± 0.5	0.35 ± 0.33 ± 0.04
−0.625 – −0.500	13.4 ± 3.9 ± 1.5	
−0.500 – −0.375	7.6 ± 6.9 ± 0.9	1.03 ± 0.46 ± 0.12
−0.375 – −0.250	18.1 ± 4.0 ± 2.0	
−0.250 – −0.125	21.2 ± 4.7 ± 2.4	1.59 ± 0.46 ± 0.19
−0.125 – 0.000	19.4 ± 4.4 ± 2.2	
0.000 – 0.125	21.7 ± 4.3 ± 2.4	1.68 ± 0.45 ± 0.20
0.125 – 0.250	20.2 ± 4.0 ± 2.3	
0.250 – 0.375	23.9 ± 3.8 ± 2.7	0.82 ± 0.41 ± 0.10
0.375 – 0.500	20.0 ± 3.9 ± 2.2	
0.500 – 0.625	18.6 ± 3.3 ± 2.1	0.68 ± 0.33 ± 0.08
0.625 – 0.750	14.5 ± 3.2 ± 1.6	

TABLE XI. The averaged invariant differential cross sections $\left(Ed^3\sigma/dp^3\right)$ as a function of rapidity and p_T for the inclusive reaction $pp \rightarrow \eta$X at 530 GeV/c. The units are pb/(GeV/c)^2.

y_{cm}	p_T (GeV/c) 4.00 – 5.00	5.00 – 6.00	6.00 – 8.00
−0.75 – −0.50	520 ± 250 ± 60	29 ± 19 ± 3	1.6 ± 1.0 ± 0.2
−0.50 – −0.25	700 ± 230 ± 80	53 ± 16 ± 6	
−0.25 – 0.00	1150 ± 190 ± 120	57 ± 16 ± 6	1.1 ± 1.0 ± 0.1
0.00 – 0.25	740 ± 150 ± 80	70 ± 18 ± 8	
0.25 – 0.50	800 ± 110 ± 90	46 ± 13 ± 5	1.3 ± 1.2 ± 0.1
0.50 – 0.75	573 ± 73 ± 61	48 ± 13 ± 5	

TABLE XII. The averaged invariant differential cross sections per nucleon $\left(Ed^3\sigma/dp^3\right)$ as a function of rapidity and p_T for the inclusive reaction pBe $\rightarrow \eta$X at 800 GeV/c. The units are pb/(GeV/c)^2.

y_{cm}	p_T (GeV/c) 3.00 – 4.00	4.00 – 4.50	4.50 – 5.00	5.00 – 5.50
−1.00 – −0.875	13000 ± 15000 ± 1000	920 ± 580 ± 100	—	116 ± 47 ± 13
−0.875 – −0.750		1360 ± 620 ± 150	500 ± 240 ± 60	87 ± 52 ± 10
−0.750 – −0.625	46000 ± 11000 ± 5000	1980 ± 630 ± 220	560 ± 130 ± 60	155 ± 43 ± 17
−0.625 – −0.500		1270 ± 580 ± 140	540 ± 160 ± 60	259 ± 48 ± 29
−0.500 – −0.375	17300 ± 8100 ± 1900	2330 ± 550 ± 260	640 ± 120 ± 70	299 ± 49 ± 34
−0.375 – −0.250		3840 ± 530 ± 420	710 ± 150 ± 80	253 ± 56 ± 29
−0.250 – −0.125	48200 ± 8800 ± 5300	3520 ± 570 ± 390	570 ± 130 ± 60	239 ± 48 ± 27
−0.125 – 0.000		4130 ± 520 ± 460	940 ± 140 ± 100	292 ± 53 ± 33
0.000 – 0.125	34500 ± 6700 ± 3800	4070 ± 600 ± 450	1200 ± 160 ± 130	311 ± 64 ± 35
0.125 – 0.250		2840 ± 510 ± 310	1220 ± 180 ± 140	386 ± 76 ± 44
0.250 – 0.375	29000 ± 7100 ± 3200	3670 ± 350 ± 410	1170 ± 130 ± 130	275 ± 57 ± 31
0.375 – 0.500		2230 ± 260 ± 250	1090 ± 110 ± 120	282 ± 48 ± 32

y_{cm}	5.50 – 6.50	6.50 – 8.00	8.00 – 10.00
−1.00 – −0.875	9 ± 10 ± 1	—	1.50 ± 0.93 ± 0.19
−0.875 – −0.750	22.5 ± 8.9 ± 2.6		
−0.750 – −0.625	51 ± 16 ± 6	6.8 ± 2.0 ± 0.8	0.52 ± 0.93 ± 0.07
−0.625 – −0.500	41 ± 11 ± 5		
−0.500 – −0.375	34 ± 12 ± 4	4.3 ± 1.6 ± 0.5	0.55 ± 0.52 ± 0.07
−0.375 – −0.250	51 ± 11 ± 6		
−0.250 – −0.125	86 ± 16 ± 10	6.4 ± 1.5 ± 0.8	0.68 ± 0.23 ± 0.09
−0.125 – 0.000	79 ± 13 ± 9		
0.000 – 0.125	93 ± 17 ± 11	8.3 ± 2.2 ± 1.0	0.61 ± 0.28 ± 0.08
0.125 – 0.250	70 ± 18 ± 8		
0.250 – 0.375	61 ± 15 ± 7	7.4 ± 1.8 ± 0.9	0.48 ± 0.27 ± 0.06
0.375 – 0.500	54 ± 13 ± 6		

TABLE XIII. The averaged invariant differential cross sections $\left(Ed^3\sigma/dp^3\right)$ as a function of rapidity and p_T for the inclusive reaction $pp \rightarrow \eta$X at 800 GeV/c. The units are pb/(GeV/c)^2.

y_{cm}	p_T (GeV/c) 4.00 – 5.00	5.00 – 6.00	6.00 – 8.00
−1.0 – −0.75	1060 ± 430 ± 120	73 ± 50 ± 8	6.9 ± 3.6 ± 0.8
−0.75 – −0.50	360 ± 520 ± 40	97 ± 49 ± 11	4.9 ± 7.1 ± 0.6
−0.50 – −0.25	1930 ± 420 ± 210	194 ± 40 ± 22	14.4 ± 7.6 ± 1.7
−0.25 – 0.00	1880 ± 440 ± 210	256 ± 47 ± 29	22.3 ± 6.0 ± 2.6
0.00 – 0.25	1980 ± 470 ± 220	167 ± 55 ± 19	16.9 ± 7.6 ± 2.0
0.25 – 0.50	1230 ± 250 ± 140	198 ± 50 ± 22	9.6 ± 5.0 ± 1.1